Molecular BioSystems

PAPER

View Article Online
View Journal | View Issue

Cite this: *Mol. BioSyst.*, 2014, **10**, 1978

Experimental design, validation and computational modeling uncover DNA damage sensing by DNA-PK and ATM†

R. J. Flassig,‡*[a] G. Maubach,‡[b] C. Täger,[b] K. Sundmacher[ac] and M. Naumann[b]

Received 17th February 2014,
Accepted 4th May 2014

DOI: 10.1039/c4mb00093e

www.rsc.org/molecularbiosystems

Reliable and efficient detection of DNA damage constitutes a vital capability of human cells to maintain genome stability. Following DNA damage, the histone variant H2AX becomes rapidly phosphorylated by the DNA damage response kinases DNA-PK$_{cs}$ and ATM. H2AX phosphorylation plays a central role in signal amplification leading to chromatin remodeling and DNA repair initiation. The contribution of DNA-PK$_{cs}$ and ATM to H2AX phosphorylation is however puzzling. Although ATM is required, DNA-PK$_{cs}$ can substitute for it. Here we analyze the interplay between DNA-PK$_{cs}$ and ATM with a computational model derived by an iterative workflow: switching between experimental design, experiment and model analysis, we generated an extensive set of time-resolved data and identified a conclusive dynamic signaling model out of several alternatives. Our work shows that DNA-PK$_{cs}$ and ATM enforce a biphasic H2AX phosphorylation. DNA-PK$_{cs}$ can be associated to the initial, and ATM to the succeeding phosphorylation phase of H2AX resulting into a signal persistence detection function for reliable damage sensing. Further, our model predictions emphasize that DNA-PK$_{cs}$ inhibition significantly delays H2AX phosphorylation and associated DNA repair initiation.

1. Introduction

Cells are constantly affected by DNA damage, resulting from ionizing γ-irradiation (IR), genotoxic or replication stress and reactive oxygen species. DNA damage, including single and double strand breaks (DSB), base modification, deletions or point mutations, seriously affects genome stability and cell integrity if not properly detected and repaired by the DNA damage response (DDR).[1]

Upon DNA damage detection, higher order chromatin has to be made accessible by various modifications before DSB can be repaired.[2] Among several DNA-damage associated histone modifications, phosphorylation of H2AX is widely accepted as an indicator of DSB. H2AX becomes rapidly phosphorylated at serine 139 (γH2AX) to generate foci at the DSB site.[3] The assembly of chromatin remodeling complexes at the DSB site greatly depends on γH2AX and enables the accessibility of the damaged DNA to repair proteins.[4]

Depending on the stimulus, γH2AX is induced by different members of the phosphoinositide 3-kinase like kinase (PIKK) family; ataxia telangiectasia mutated (ATM), ataxia telangiectasia and Rad3-related (ATR) and DNA-dependent protein kinase catalytic subunit (DNA-PK$_{cs}$). ATR phosphorylates H2AX upon replicative stress,[5] whereas ATM and DNA-PK$_{cs}$ are responsible for this phosphorylation upon DNA DSB, which are induced by IR.[6] ATM and DNA-PK$_{cs}$ have been studied on a qualitative basis focusing on their impact of repair pathway choice for rebuilding damaged DNA either *via* rapid (classical) non-homologous end joining cNHEJ and/or slow homologous recombination repair (HR) pathway.[7,8] As for the pathway choice, the interplay between ATM and DNA-PK$_{cs}$ regarding IR-induced H2AX phosphorylation remains puzzling. Because although ATM is required,[9] DNA-PK$_{cs}$ can substitute for it.[10]

In this work we follow a model-based approach to analyze the contribution of DNA-PK$_{cs}$ and ATM to H2AX phosphorylation during the initial DNA damage sensing stage. Cucinotta *et al.*[11] have created a dynamic model solely focused on DNA-PK$_{cs}$ to predict dose and dose-rate effects on γH2AX dynamics. Very recently, a mechanistic model describing DNA damage complexity dependent sub-pathway choice in cNHEJ repair has

[a] *Process Systems Engineering Group, Max Planck Institute for Dynamics of Complex Technical Systems, Magdeburg, Germany. E-mail: flassig@mpi-magdeburg.mpg.de*
[b] *Institute of Experimental Internal Medicine, Otto von Guericke University, Magdeburg, Germany*
[c] *Process Systems Engineering Group, Otto von Guericke University, Magdeburg, Germany*

† Electronic supplementary information (ESI) available: Experimental data supporting the results of this article, a detailed description on data processing, model equations, parameter estimation, values and confidence intervals, identifiability and model analysis as well as the data are provided in the supplementary material. See DOI: 10.1039/c4mb00093e

‡ Both authors contributed equally.

been presented.[12] Although several other mechanistic models of DNA-PK$_{cs}$ and cNHEJ repair exist,[13–16] mechanistic modeling of ATM dynamics in the context of DNA damage is rare.[17]

A computational model for ATM and DNA-PK$_{cs}$ interactions with regard to γH2AX activation integrating biochemical time course data is missing so far. We describe an iterative workflow to identify a predictive dynamic model involving ATM/DNA-PK$_{cs}$ mediated H2AX phosphorylation. Starting from several models, optimal experimental design (OED) was applied to optimize experiments for model identification. The identified model was used to analyze the dynamic contribution of ATM and DNA-PK$_{cs}$ to H2AX phosphorylation.

2. Results

2.1 Model identification

2.1.1 Defining network structures for γH2AX activation upon IR. The network structures (Fig. 1A) have been constructed based on meta-analysis[7,17–20] focusing on the initial activation

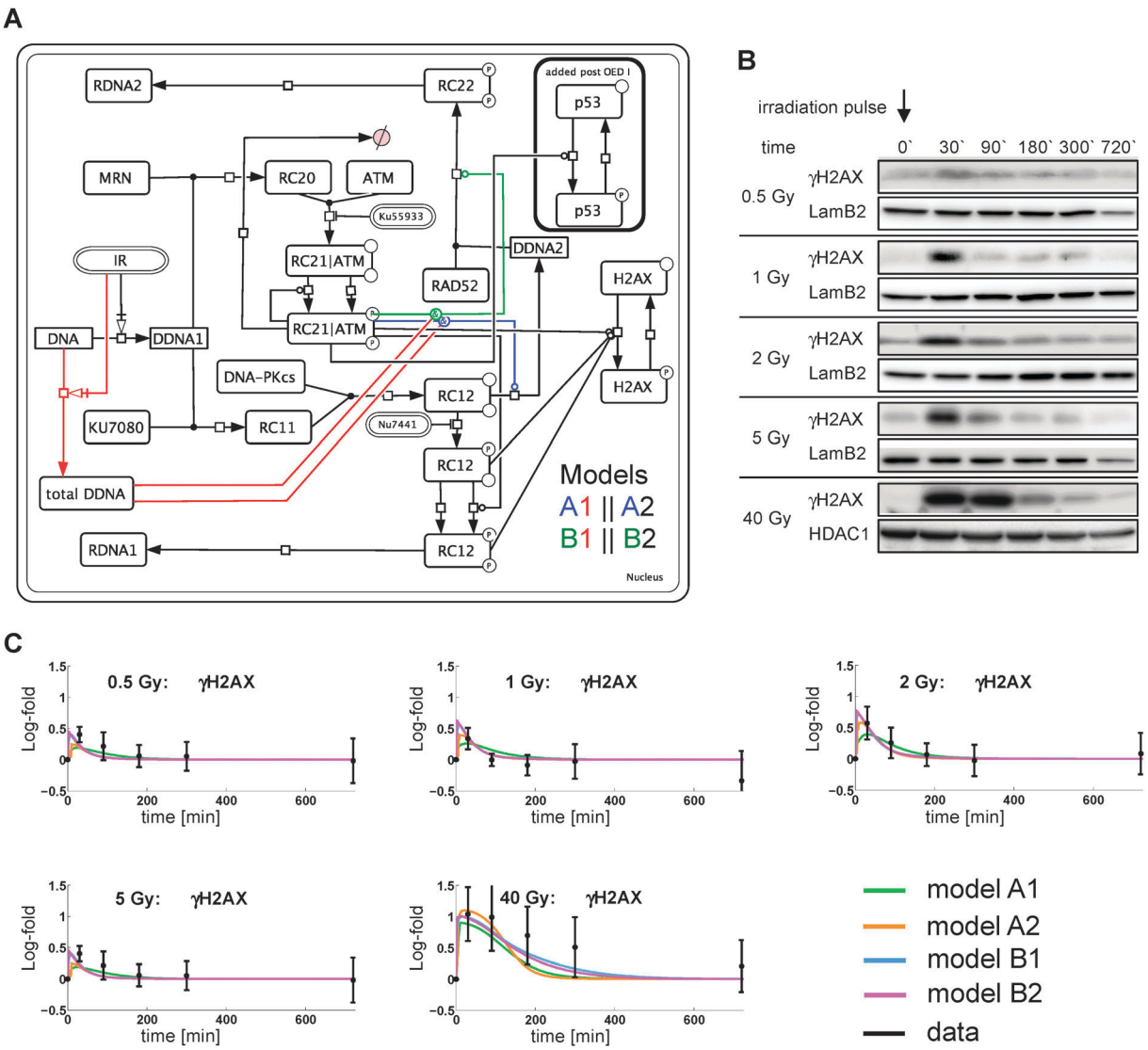

Fig. 1 Network structure and initial data (OED 0). (A) The network structures of four different models based on meta-analysis is shown as an interaction graph. Interactions are modeled *via* state transitions (arrows with squares), enzyme catalysis (lines with circles) and complex formation (joined lines). Stimulus and inhibitors have round-edge boxes. Abbreviations: IR ionizing irradiation; DDNA1 initial, damaged DNA; RC11 Ku70/80 to DDNA1 association; RC12 Ku70/80-DNA-PK$_{cs}$ complex; RDNA1/2 repaired DNA (cNHEJ/aNHEJ or HR); RC20 MRN complex to DDNA1 association; RC21|ATM MRN-ATM complex at damage site; RC22 RAD52 mediated repair complex; DDNA2, unsuccessful cNHEJ repair moved to aNHEJ/HR. Four mechanisms have been considered for branching (A1, A2, B1, B2). A and B refer to the location of the catalytic activity of ATM and indices 1 and 2 refer to the kinetic law used. For model index 1 branching to DDNA2 is catalyzed by the total amount of damaged DNA. Index 2 does not use the total amount of damaged DNA. (B) MDCK cells were irradiated with different doses and the insoluble nuclear extracts were analyzed by immunoblot. Lamin B2 or HDAC1 served as loading control. (C) Model simulation and quantified experimental data for OED 0 using the estimated band intensities of γH2AX. Data represent mean ± 2SD of 3–5 independent experiments.

dynamic within the nucleus and the interplay between ATM and DNA-PK$_{cs}$. DDR initiates with recognition of damaged DNA (DDNA1). Ku70/80 as a sensor for cNHEJ associates to the damage site (RC11) forming the DNA-PK complex (RC12).[21] Then, the catalytic subunit of DNA-PK is either phosphorylated by active ATM or/and autophosphorylated at the T2609 cluster to initiate cNHEJ.[8] The MRN complex (Mre11-Rad50-Nbs1), a sensor for the HR pathway, can also co-localize to the damage site to promote ATM autophosphorylation at Ser1981.

Failure of DNA repair *via* cNHEJ potentially allows HR proteins to access the damage site. This is modeled by splitting the initial DSB pool (DDNA) into DDNA1 and DDNA2, whereby DDNA2 is associated to HR and/or alternative non-homologous end joining (aNHEJ).[22] Phosphorylation of H2AX can be achieved by active DNA-PK$_{cs}$ or active ATM. We generated four alternative models describing various interplays between ATM, DNA-PK$_{cs}$ and γH2AX (Fig. 1A).

2.1.2 Experimental design for model calibration and identification. For model calibration purpose, an initial time course of H2AX phosphorylation in response to IR was studied in MDCK cells in a dose-dependent manner using 0.5, 1, 2, 5, 40 Gy. γH2AX levels increased with IR dose, while concurrently signal attenuation was delayed (Fig. 1B). These results agree with data from Burma *et al.*[9] From the competing network structures, we derived ordinary differential equation models and calibrated them (see Materials and methods). Simulations of the initial data set for all models are shown in Fig. 1C. Based on χ^2 statistics, none of the models could be rejected at a significance level of $\alpha_{0.05} = 0.05$ (Table 1, OED 0). *p*-Values of Anderson–Darling (AD) residual statistics also indicated that all models seemed adequate for the initial data.

To discriminate between models, we subsequently designed (i) an IR double-pulse (Fig. 2A–D) and (ii) an IR double-pulse in combination with kinase inhibitors (Fig. 3). The IR double-pulse was parameterized with 2 design variables, namely inter-pulse time D_1 and second pulse dose D_2, whereas the first pulse was fixed at 1 Gy. The objective was to maximize $O = [T_{red}\langle V\rangle\langle S\rangle]^T$. Herein T_{red} is the reduced, modified T criterion to measure discriminative power,[23] whereas $\langle V\rangle$, $\langle S\rangle$ represent mean model prediction variance and variance-entropy. The latter two criteria measure parameter information and distribution within the γH2AX signal (see Materials and methods).

For OED I, the optimal design $\mathbf{D}_I^*$ was chosen by trading off T_{red}, $\langle V\rangle$ and $\langle S\rangle$ (Fig. 2B). Recalibration of all models to data from OED 0 and I, and additional inclusion of p53-P data (Fig. 2E) from titration experiments did not allow for model discrimination (all *p*-values $> \alpha_{0.05}$ for both fit statistics; Table 1), but reduced prediction variances (Table 2).

Kinase inhibitors were employed for OED II to better dissect DNA-PK$_{cs}$ and ATM contributions. Titration of two highly specific inhibitors, namely Nu7441 and Ku55933 for DNA-PK$_{cs}$ and ATM, respectively, identified the optimal concentration for each. Further, we used the phosphorylation of p53 at S15 as a read-out to show the specificity of the inhibitors. Two successive pulses with different intensities (1 and 20 Gy) show in the immunoblot that the contribution of DNA-PK$_{cs}$ to this particular phosphorylation of p53 is marginal (Fig. 2E). This confirms earlier data.[24,25]

OED II was designed for three different inhibitor settings, namely Nu7441 and/or Ku55933. The estimated optimal design $\mathbf{D}_{II}^*$ potentially allowed for discrimination (Table 2, $T_{red}^* \gg 1$, Fig. 3A). The initial γH2AX peak showed a comparable reduction for both inhibitors. Phosphorylation of H2AX after the second pulse seemed to decay more rapidly for inhibited ATM compared to inhibited DNA-PK$_{cs}$. Both inhibitors together showed synergistic effects on γH2AX (Fig. 3B).

According to the fit statistics of OED II (Table 1) only model A2 cannot be rejected in terms of χ^2. However, we find significant AD *p*-values for all four models, whereas models A2 and B2 have non-significant AD$_{3\sigma}$ *p*-values, which account only for residuals smaller than 3σ. This behavior may be attributed to outliers in one of the experimental conditions (Fig. 1C and 3C) owing to experimental variations or deficits of the models in describing experimental conditions of OED 0, I, II. We selected model A2 as the final model for further analysis, since it was the only model with *p*-values of χ^2 and AD$_{3\sigma}$ statistics exceeding $\alpha_{0.05}$ for all 3 experimental runs.

Table 1 Fit statistics for initial (OED 0) and optimized experiments (OED I and II) Anderson–Darling *p*-values are indicated as AD. AD$_{3\sigma}$ indicates *p*-values of AD statistics where residuals larger than 3σ have been excluded. The number of data points N_{data} do not include the time point $t = 0$ [min]. N_θ and N_S indicate the number of estimated kinetic and scaling parameters

OED	N_{data}	N_θ	N_S	Fit statistics	Model A1	Model A2	Model B1	Model B2
0	114	19	2	χ^2	93.45	91.74	92.79	91.69
				p-Value χ^2	4.09×10^{-01}	4.59×10^{-01}	4.28×10^{-01}	4.60×10^{-01}
				p-Value AD$_{3\sigma}$	3.44×10^{-02}	1.21×10^{-02}	3.04×10^{-02}	2.32×10^{-02}
				p-Value AD	3.44×10^{-02}	1.21×10^{-02}	3.04×10^{-02}	2.32×10^{-02}
I	147	19	7	χ^2	135.98	131.53	125.84	125.64
				p-Value χ^2	1.37×10^{-01}	2.04×10^{-01}	3.16×10^{-01}	3.21×10^{-01}
				p-Value AD$_{3\sigma}$	1.38×10^{-01}	1.84×10^{-01}	9.22×10^{-02}	5.64×10^{-02}
				p-Value AD	2.12×10^{-01}	1.84×10^{-01}	9.22×10^{-02}	5.64×10^{-02}
II	237	19	8	χ^2	290.60	208.2	286.22	479.10
				p-Value χ^2	1.35×10^{-04}	4.83×10^{-01}	2.60×10^{-04}	0.00
				p-Value AD$_{3\sigma}$	1.97×10^{-05}	6.52×10^{-02}	3.11×10^{-02}	1.12×10^{-01}
				p-Value AD	3.86×10^{-08}	5.22×10^{-29}	3.21×10^{-32}	5.46×10^{-14}

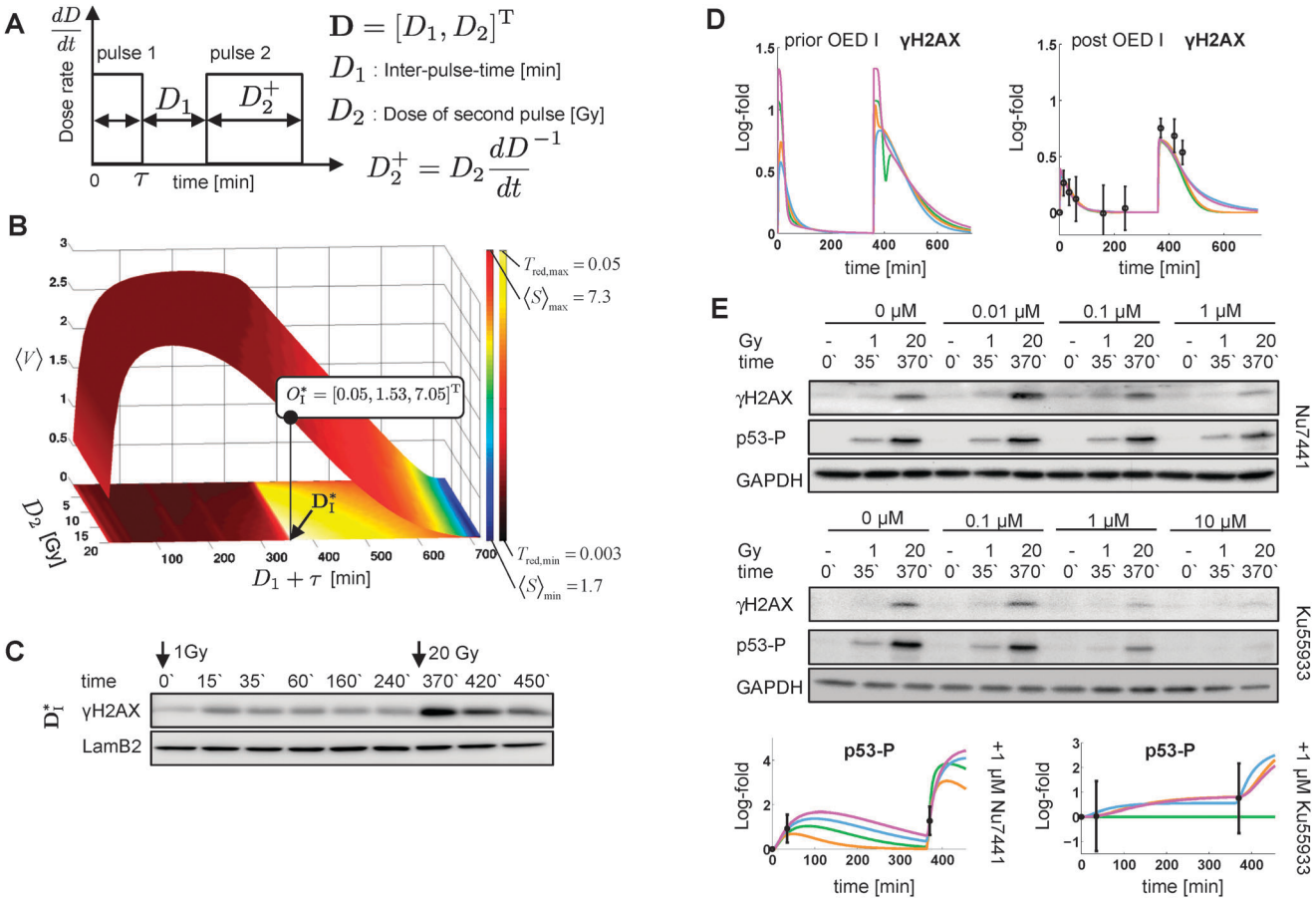

Fig. 2 Parameterization of the stimulus design, design criteria and respective immunoblots. (A) Parameterization of the stimulus design for OED I/II. (B) Design criteria predicted from the model simulations are plotted over the feasible design space. The optimal design point for OED I $\mathbf{D}_I$* and corresponding criteria O_I* = $[T_{red}\langle V\rangle\langle S\rangle]^T$ are indicated. (C) A representative immunoblot from an experiment based on $\mathbf{D}_I$* is shown. MDCK cells were irradiated as indicated and the insoluble nuclear extracts were analyzed by immunoblot. Lamin B2 served as loading control. (D) Corresponding model simulation describe the acquired data for γH2AX (model colors as in Fig. 1). Data represent mean ± 2SD of 3 independent experiments. (E) MDCK cells were irradiated as indicated. Inhibitors Ku55933 and Nu7441 were used at different concentrations and whole cell lysates were analyzed for p53-P and γH2AX. GAPDH served as loading control. Model simulation and quantified experimental data for p53-P are shown. Data of a single experiment.

2.2 Model predictions

2.2.1 Biphasic control of H2AX phosphorylation by DNA-PK$_{cs}$ and ATM. To investigate the contribution of DNA-PK$_{cs}$ and ATM to H2AX phosphorylation, we analyze their times of maximal peak activity post irradiation. We simulated a single IR pulse from 1 mGy to 100 Gy (Fig. 4A–C). Active DNA-PK$_{cs}$ (DNA-PK$_{cs}$-P) responds directly after irradiation within 2–10 minutes and shows fast signal attenuation. Response time of active ATM (ATM-P) in terms of maximal activity is delayed with respect to γH2AX and much more dose-dependent ranging from 10 to 56 minutes. These model predictions are in line with the literature: DNA-PK$_{cs}$ activation peaks at 10 minutes after IR treatment, whereas ATM has its peak activity at around 20 minutes.[26]

According to the model predictions, phosphorylation of H2AX is biphasic, following a dose-independent temporal activation order: the first activation phase of γH2AX right after stimulation is associated to DNA-PK$_{cs}$, whereat the second phase is linked to ATM-P (Fig. 4A). The γH2AX signal decays on the scale of hours and correlates with ATM-P. This dynamics of fast initial and prolonged response is known from coherent feed forward loops, which serve as a signal persistence detector.[27] At doses below 1 dGy peak level of γH2AX is dominated by DNA-PK$_{cs}$, whereas ATM dominates above 1 dGy (Fig. 4B and C). For larger dose levels, ATM auto-phosphorylation results into a prolonged activation phase, with γH2AX peak activity shifted from 10 minutes at 10 Gy to 40 minutes at 100 Gy.

2.2.2 DNA-PK$_{cs}$ compensates inhibited ATM. Simulations of γH2AX dynamics with inhibited DNA-PKcs or/and ATM show that exclusive inhibition of ATM is nearly compensated by DNA-PK$_{cs}$ replacing the ATM associated activation phase of γH2AX by a prolonged DNA-PK$_{cs}$ associated phase (Fig. 5A left and B black *vs.* magenta). In contrast, DNA-PK$_{cs}$ inhibition results into loss of the DNA-PK$_{cs}$ associated activation phase. Owing to slower activation kinetics, ATM cannot compensate this delay (Fig. 5A left and B black *vs.* red). At doses where DNA-Pk$_{cs}$ dominates, γH2AX peak activity is delayed by roughly 45 minutes. Simulations of simultaneous inhibition of DNA-PK$_{cs}$ and ATM show a 3- to 10-fold reduction in γH2AX peak level, depending on IR dosage, whereas exclusive inhibition of either DNA-PK$_{cs}$ or ATM is not as much

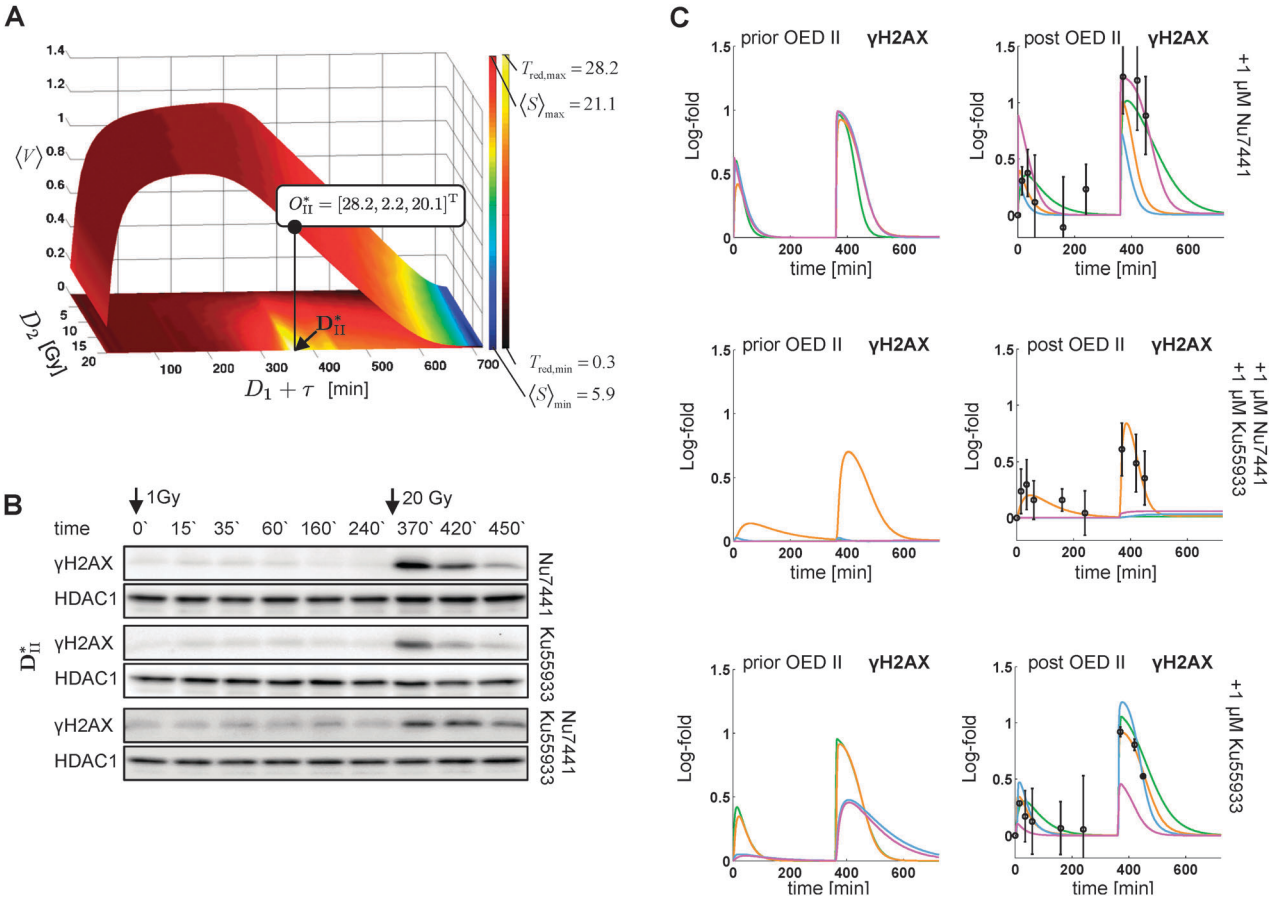

Fig. 3 (A) $\mathbf{D}_{II}$* is obtained as in Fig. 2(B). (B) MDCK were incubated with 1 μM of the indicated inhibitor and irradiated as indicated. The insoluble nuclear extracts were analyzed by immunoblot. HDAC1 served as loading control. (C) The corresponding model simulations compare the acquired data for γH2AX before and after OED II (mean ± 2SD of 2–4 independent experiments, model colors as in Fig. 1).

Table 2 Design criteria for OED $\langle V \rangle$ and $\langle S \rangle$ represent mean variance and variance-entropy over all models, time points and specific experimental conditions (initial = subscript 0, OED I, II)

	OED I		OED II	
Criterion	Prediction	Final	Prediction	Final
$T^*\|T_0^*$	107.13|6.5	45.1|0.3	4.6×10^{-03}|44.7	1.5×10^{-03}|51.5
$T_{red}^*\|T_{red,0}^*$	0.05|3×10^{-3}	0.02|1×10^{-04}	28.2|0.3	9.3|0.3
$\langle V \rangle\|\langle V \rangle_0$	1.53|4×10^{-08}	0.52|2×10^{-07}	2.2|6×10^{-08}	0.6|1×10^{-05}
$\langle S \rangle\|\langle S \rangle_0$	7.05|2.26	7|2.29	20.1|7.5	5.1|3.1

affecting peak activity of γH2AX (Fig. 5A right). For all inhibition scenarios, the biphasic phosphorylation kinetics of H2AX is lost.

3. Materials and methods

3.1 Cell culture and treatment with γ-irradiation

MDCK cells (ATCC CCL-34) were routinely cultured in RPMI-1640 supplemented with 10% fetal calf serum, glutamine and 100 U mL^{-1} penicillin and 100 μg mL^{-1} streptomycin, and incubated at 37 °C in a 5% CO_2 humidified incubator. The MDCK cells were seeded at a density of 2×10^6 per 10 cm culture dish and cultured for 24 hours. The cells were irradiated with the Biobeam GM 2000 (Gamma-Service Medical GmbH, Germany) at a dose rate of 3.332 Gy min^{-1} using either single or double-pulse conditions. After a single pulse of 40, 5, 2, 1 or 0.5 Gy, the cells were harvested at 30, 90, 180, 300 and 720 minutes. The double-pulse consists of a single pulse of 1 Gy, followed 6 hours later by a second pulse of 20 Gy. The cells were harvested at 15, 35, 60, 160, 240, 370, 420 and 450 minutes. The inhibitors, Ku55933 (ATM, Tocris Bioscience, Germany) and Nu7441 (DNA-PK_{cs}, Tocris Bioscience, Germany), used in the double-pulse setting, were added 30 minutes before first irradiation at a final concentration of 1 μM, either alone or together. The titration of the inhibitors were performed at 0,

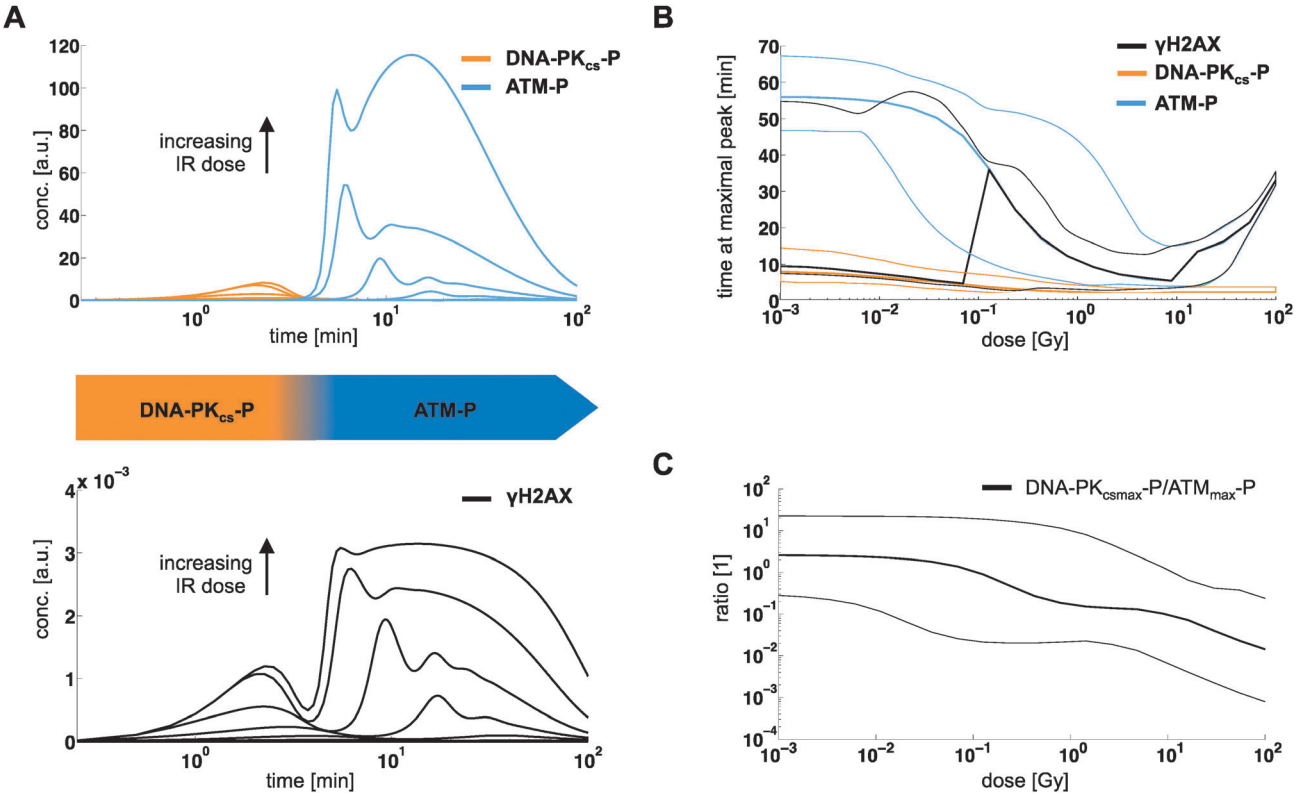

Fig. 4 Model predictions for the dynamic contribution of DNA-PK_{cs} and ATM to γH2AX. (A) Simulated time courses of active DNA-PK_{cs} and ATM and resulting biphasic γH2AX activity for IR pulses of different dose levels (1 mGy to 100 Gy). At larger dose, ATM shows a damped oscillation as a result of a positive feedback (autophosphorylation), which contributes to peak level of γH2AX at doses above 10 Gy. (B) Model prediction of the corresponding dose response in terms of time points at maximal activity of γH2AX, DNA-PK_{cs} and ATM. Thin lines indicate 95% confidence regions of the model predictions, estimated from simulations along the profile likelihood. (C) Ratio of maximal DNA-PK_{cs}-P to ATM-P. Thin lines indicate 95% confidence region of the model predictions, estimated as in (B).

0.1, 1, 10 and 0, 0.01, 0.1, 1 μM for Ku55933 and Nu7441, respectively. Both inhibitors belong to the class of ATP competitive inhibitors.[10,28]

3.2 Nuclear extraction, SDS-PAGE and Immunoblot

Cells were lysed in hypotonic cell lysis buffer (20 mM Tris/HCl pH 7.9, 10 mM KCl, 1.5 mM $MgCl_2$, 10 mM K_2HPO_4, 10% glycerol, 0.5 mM DTT) supplemented with 0.5 mM AEBSF, 1 mM sodium vanadate, 1 mM sodium molybdate, 10 mM sodium fluoride, 20 mM 2-phosphoglycerate and protease inhibitor mix (complete, Roche Germany). After addition of 1.25% NP-40, the cytosolic fraction was obtained by centrifugation at 13 000 × *g* for 10 minutes. The nuclear pellet was resolved in 20 mM Tris/HCl pH 7.9, 420 mM KCl, 1.5 mM $MgCl_2$, 10 mM K_2HPO_4, 10% glycerol, 0.2 mM EDTA, 0.5 mM DTT supplemented with the same inhibitors as before. The sample was incubated for 40 minutes on ice and centrifuged for 10 minutes at 13 000 × *g*. The insoluble nuclear fraction was achieved by digesting the resulting pellet with nuclease (Calbiochem, Germany) at 37 °C for 30 minutes. The protein concentration was estimated using the BCA protein assay kit (Perbio Science, Germany). The samples were separated in Tris-Glycine gels (15%), transferred onto PVDF membranes (Millipore, Germany) and blocked for 1 h at room temperature with 5% skim milk in TBS-Tween (TBS-T). The primary antibodies were incubated overnight in 5% skim milk in TBS-T at 4 °C. The membranes were washed thrice in TBS-T. The appropriate HRP-conjugated secondary antibody was added at a dilution of 1 : 5000 in 5% skim milk in TBS-T for 1 hour at room temperature, followed by three washes in TBS-T. The membranes were developed using a chemiluminescence substrate (Millipore, Germany). The respective bands were visualized using the ChemoCam Imager (Intas, Germany), followed by the estimation of the band intensities using ImageJ.[29]

Antibodies used in this work were as follows: LaminB2 (sc-133722) and HDAC1 (sc-7872) were obtained from Santa Cruz (USA, CA). γH2AX (ab26350) was from Abcam (UK). The secondary anti-rabbit-HRP or anti-mouse-HRP antibodies were from Jackson ImmunoResearch Laboratories Inc. (USA, PA).

3.3 Building of a dynamic signaling model network of γH2AX activation

Initially, 4 dynamic models in the form of ordinary differential equation systems were derived from the network structures in Fig. 1A and implemented in MATLAB using the solver CVODES.[30] Details on the choice of kinetic rate laws are given in the ESI† Section S2. After the poor discrimination performance of OED I, we extended the models to contain also p53. The tumor suppressor p53 is an important effector protein during DDR. Phosphorylation of p53

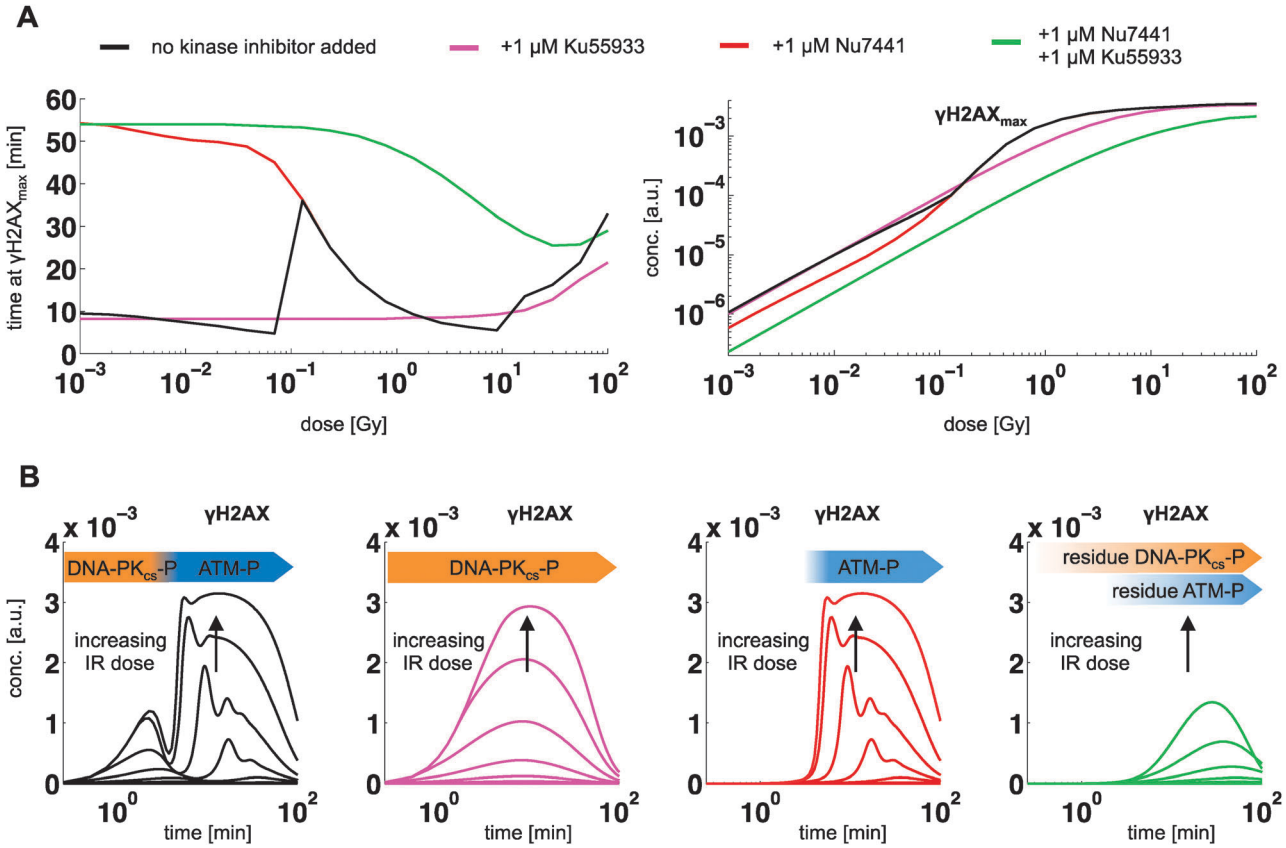

Fig. 5 Model predictions for the dynamic contribution of DNA-PK$_{cs}$ and ATM to γH2AX at inhibition for different dose levels (1 mGy to 100 Gy). (A) Peak time and peak level of γH2AX for indicated inhibitors (color code), (B) corresponding time courses.

at Ser15 by ATM promotes its release from MDM2 and results in p53 activation.[24,31] Activation of p53 by DNA-PK$_{cs}$ has also been described.[32] However, DNA-PK$^{-/-}$ MEFs show normal p53 activation.[25] We did not find evidence for a DNA-PK$_{cs}$ contribution to the p53 phosphorylation (Fig. 2E), which agrees with earlier data.[33] Therefore, we implemented the p53 activation as an ATM-dependent process only. As described in detail in the ESI,† 19 kinetic and 8 scaling parameters were estimated by maximizing the likelihood function, whereas the variance has been estimated from data replicates. Parameter estimation was performed for each model in an iterative manner, according to the 3 datasets, OED 0/I/II. Optimization of the likelihood function was performed iteratively, using a hybrid strategy. We combined a genetic algorithm ('ga' function from the global optimization toolbox of MATLAB), which was used to obtain a population of suitable starting solutions for a local, gradient-based optimization. Here we used an interior-point algorithm ('fmincon' function from the optimization toolbox of MATLAB).

Before analyzing DNA-PK$_{cs}$, ATM and γH2AX dynamics with model A2, we performed an identifiability analysis based on the profile likelihood to assess the uniqueness of the model prediction and to also derive prediction uncertainty bands (see Fig. 4B and C). This analysis revealed that 8 kinetic parameters were not fully identifiable for the given optimization constraints, *i.e.* upper and lower bounds restricting the parameters to fall within 4 orders of magnitude. Six of these parameters were non-significant at the upper bound, whereas the other two were non-significant at the lower bound. One parameter was structurally non-identifiable. The non-identifiable parameters were not decisive for the question of kinase contribution to H2AX phosphorylation. More details on the identifiability analysis, parameter dependencies and impact on the prediction power are given in the ESI† in Section 2.

3.4 Experimental design criteria for model identification

Model identification is the process of comparing plausibility amongst models from a pool of competing computational models in the light of given experimental data. Plausibility is typically derived from some kind of lack-of-fit measure, for instance χ^2 statistics. Experimental design for model identification aims at generating new experimental conditions and therefore data, to support this identification process in an optimal way using the models at hand. In the early phase of modeling a biochemical system with ODEs, parameters are typically very uncertain. Consequently, model predictions including design criteria are uncertain as well. Accounting for these uncertainties during design robustifies the optimal experiment against these uncertainties. In this work we use a multi criterion approach to identify optimal stimulus designs for model identification. We use three criteria that measure discriminative power, parameter information and its distribution along the time points of the model predictions for γH2AX.

The discriminative power is measured with the reduced, modified T criterion,[23] $T_{\mathrm{red}} = \frac{1}{N_{\mathrm{M}} N_{\mathrm{t}}} \sum_{i=1}^{N_{\mathrm{M}}-1} \sum_{j=i+1}^{N_{\mathrm{M}}} T_{ij}(\mathbf{D})$, with $T_{ij}(\mathbf{D}) = \sum_{l=1}^{N_{\mathrm{t}}} \frac{\left(\langle y_{\mathrm{sim},i}(t_l, \mathbf{D})\rangle - \langle y_{\mathrm{sim},j}(t_l, \mathbf{D})\rangle\right)^2}{2\sigma_{\mathrm{exp}}{}^2(t_l) + \sigma_{\mathrm{sim},i}{}^2(t_l, \mathbf{D}) + \sigma_{\mathrm{sim},j}{}^2(t_l, \mathbf{D})}$, where $\langle y_{\mathrm{sim},i}(t_l, \mathbf{D})\rangle$ represents the expected prediction of γH2AX of model i (total number N_{M}) at time point t_l (total number N_{t}). Measurement variances $\sigma_{\mathrm{exp}}{}^2(t_l)$ are interpolated sample variances averaged over all available experimental conditions. Expected model predictions and their variances $\sigma_{\mathrm{sim},i}{}^2(t_l, \mathbf{D})$ have been derived with the sigma point method as shown in Flassig and Sundmacher.[34] Expectation is taken with respect to the parameters, whereas parameter variance–covariances were derived from the χ^2 Hessian. Parameter information was measured by the mean variance over time points of model predictions according to $\langle V\rangle = \frac{1}{N_{\mathrm{t}} N_{\mathrm{M}}} \sum_{i=1}^{N_{\mathrm{t}}} \sum_{j=1}^{N_{\mathrm{M}}} \sigma_{\mathrm{sim},j}{}^2(t_i, \mathbf{D})$. Shannon's entropy is used to measure the variance distribution over time points and model predictions according to $\langle S\rangle = \sum_{j=1}^{N_{\mathrm{M}}} \sum_{i=1}^{N_{\mathrm{t}}} -\tilde{\sigma}_{\mathrm{sim},j}{}^2(t_i, \mathbf{D}) \log \tilde{\sigma}_{\mathrm{sim},j}{}^2(t_i, \mathbf{D})$ with normalized variances according to $\sum_{j=1}^{N_{\mathrm{M}}} \sum_{i=1}^{N_{\mathrm{t}}} \tilde{\sigma}_{\mathrm{sim},j}{}^2(t_i, \mathbf{D}) = 1$. In each experimental design, we chose the best design point as the trade-off between maximal T_{red}, $\langle V\rangle$ and $\langle S\rangle$. Maximal T_{red} yields best discrimination, maximal $\langle V\rangle$ ensures large sensitivity of the parameters and maximal $\langle S\rangle$ represents maximal homogenous variance distribution along time points and model predictions.

The evaluation of the objective in OED I was based on time points $t = [0\ 15\ 35\ 60\ 160\ 240\ 370\ 420\ 450]^{\mathrm{T}}$ minutes. The first 6 time points were chosen from simulating OED 0 conditions to fully capture rising and falling flanks of the initial γH2AX peak, whereas the remaining time points were placed based on the estimated second signal peak. For OED II design criteria were evaluated at the time points used in OED I.

4. Conclusions

Here we report an iterative workflow combining experimental work, computational modeling and experimental design methodologies to shed light on the interplay of two PIKK family members (DNA-PK$_{\mathrm{cs}}$ and ATM) to the rapid histone H2AX phosphorylation in the context of DNA damage sensing upon γ-irradiation. By performing optimized dynamic stimulation experiments, we generated an extensive set of time-resolved data to identify a computational model for analyzing DNA-PK$_{\mathrm{cs}}$-P, ATM-P and γH2AX dynamics. A parameter identifiability analysis revealed that the computational model can be used to predict internal state dynamics, *e.g.* phosphorylation of DNA-PK$_{\mathrm{cs}}$ and ATM. With a predictive model at hand, we could then investigate the fast phosphorylation kinetics of DNA-PK$_{\mathrm{cs}}$, ATM and H2AX post irradiation without the need of direct kinase activity measurements, thus reducing confounding effects from experimental manipulations.

Our model simulations show that H2AX phosphorylation is biphasic, with initial and succeeding phases associated to DNA-PK$_{\mathrm{cs}}$ and ATM, respectively, in which the individual contributions to peak level of γH2AX are dose-dependent. It is tempting to link the dose-dependent biphasic response of γH2AX observed *in silico* to the known biphasic signaling responses of cNHEJ and HR, that is fast DNA-PK$_{\mathrm{cs}}$ and slower ATM-related repair activity.[22] In fact, following DNA-PK$_{\mathrm{cs}}$ inhibition Davidson *et al.*[35] have shown that HR activity is increased. Further, Neal *et al.*[8] showed that DNA-PK$_{\mathrm{cs}}$ enzymatic activity inhibits HR in a titratable fashion. From simulating DNA-PK$_{\mathrm{cs}}$ inhibition we hypothesize that this is a consequence of delayed γH2AX activation, associated chromatin remodeling and DNA repair initiation of cNHEJ. We further conclude that DNA-PK$_{\mathrm{cs}}$ and ATM have distinct roles in H2AX phosphorylation equipping cells with a signal persistence detection function, *i.e.* fast initial response (DNA-PK$_{\mathrm{cs}}$) and delayed signal attenuation (ATM). This ensures reliable damage detection and repair signaling.

Author contribution

RF performed data processing, statistical analysis and computational modeling. GM performed experiments and quantified data. CT performed the experiments. KS and MN designed the research concept. RF, GM, KS and MN wrote the manuscript.

Acknowledgements

This work was supported by the German Federal Ministry of Education and Research (SysTec, 101-31P5900) and the Ministry of Education of Saxony-Anhalt (XD3639HP/0306).

References

1 A. Ciccia and S. J. Elledge, *Mol. Cell*, 2010, **40**, 179–204.
2 M. J. Kruhlak, A. Celeste, G. Dellaire, O. Fernandez-Capetillo, W. G. Müller, J. G. McNally, D. P. Bazett-Jones and A. e. Nussenzweig, *J. Cell Biol.*, 2006, **172**, 823–834.
3 J. Yuan, R. Adamski and J. Chen, *FEBS Lett.*, 2010, **584**, 3717–3724.
4 M. Stucki and S. P. Jackson, *DNA Repair*, 2006, **5**, 534–543.
5 I. M. Ward and J. Chen, *J. Biol. Chem.*, 2001, **276**, 47759–47762.
6 H. Wang, M. Wang, H. Wang, W. Bocker and G. Iliakis, *J. Cell. Physiol.*, 2005, **202**, 492–502.
7 M. Shrivastav, C. A. Miller, L. P. De Haro, S. T. Durant, B. P. C. Chen, D. J. Chen and J. A. Nickoloff, *DNA Repair*, 2009, **8**, 920–929.
8 J. A. Neal, V. Dang, P. Douglas, M. S. Wold, S. P. Lees-Miller and K. Meek, *Mol. Cell. Biol.*, 2011, **31**, 1719–1733.
9 S. Burma, B. P. Chen, M. Murphy, A. Kurimasa and D. J. Chen, *J. Biol. Chem.*, 2001, **276**, 42462–42467.
10 I. Hickson, Y. Zhao, C. J. Richardson, S. J. Green, N. M. B. Martin, A. I. Orr, P. M. Reaper, S. P. Jackson, N. J. Curtin and G. C. M. Smith, *Cancer Res.*, 2004, **64**, 9152–9159.

11 F. A. Cucinotta, J. M. Pluth, J. A. Anderson, J. V. Harper and P. O'Neill, *Radiat. Res.*, 2008, **169**, 214–222.
12 Y. Li, P. Reynolds, P. O'Neill and F. A. Cucinotta, *PLoS One*, 2014, **9**, e85816.
13 W. Friedland, P. Jacob and P. Kundrát, *Radiat. Prot. Dosim.*, 2011, **143**, 542–548.
14 R. Taleei and H. Nikjoo, *Radiat. Res.*, 2013, **179**, 530–539.
15 D. Dolan, G. Nelson, A. Zupanic, G. Smith and D. Shanley, *PLoS One*, 2013, **8**, e55190.
16 W. Friedland, P. Jacob and P. Kundrát, *Radiat. Res.*, 2010, **173**, 677–688.
17 K. Mouri, J. C. Nacher and T. Akutsu, *PLoS One*, 2009, **4**, e5131.
18 E. Mladenov and G. Iliakis, *Mutat. Res., Fundam. Mol. Mech. Mutagen.*, 2011, **711**, 61–72.
19 A. Kinner, W. Wu, C. Staudt and G. Iliakis, *Nucleic Acids Res.*, 2008, **36**, 5678–5694.
20 R. Poltz and M. Naumann, *BMC Syst. Biol.*, 2012, **6**, 125.
21 D. W. Chan, B. P.-C. Chen, S. Prithivirajsingh, A. Kurimasa, M. D. Story, J. Qin and D. J. Chen, *Genes Dev.*, 2002, **16**, 2333–2338.
22 J. A. Neal and K. Meek, *Mutat. Res., Fundam. Mol. Mech. Mutagen.*, 2011, **711**, 73–86.
23 G. Buzzi-Ferraris and P. Forzatti, *Chem. Eng. Sci.*, 1983, **38**, 225–232.
24 C. E. Canman, D. S. Lim, K. A. Cimprich, Y. Taya, K. Tamai, K. Sakaguchi, E. Appella, M. B. Kastan and J. D. Siliciano, *Science*, 1998, **281**, 1677–1679.
25 G. S. Jimenez, F. Bryntesson, M. I. Torres-Arzayus, A. Priestley, M. Beeche, S. Saito, K. Sakaguchi, E. Appella, P. A. Jeggo, G. E. Taccioli, G. M. Wahl and M. Hubank, *Nature*, 1999, **400**, 81–83.
26 D. Davidson, L. Amrein, L. Panasci and R. Aloyz, *Front. Pharmacol.*, 2013, **4**, DOI: 10.3389/fphar.2013.00005.
27 S. Mangan and U. Alon, *Proc. Natl. Acad. Sci. U. S. A.*, 2003, **100**, 11980–11985.
28 J. J. J. Leahy, B. T. Golding, R. J. Griffin, I. R. Hardcastle, C. Richardson, L. Rigoreau and G. C. M. Smith, *Bioorg. Med. Chem. Lett.*, 2004, **14**, 6083–6087.
29 C. A. Schneider, W. S. Rasband and K. W. Eliceiri, *Nat. Methods*, 2012, **9**, 671–675.
30 A. Hindmarsh, P. Brown, K. Grant, S. Lee, R. Serban, D. Shumaker and C. Woodward, *ACM Trans. Math. Softw.*, 2005, **31**, 363–396.
31 S.-Y. Shieh, M. Ikeda, Y. Taya and C. Prives, *Cell*, 1997, **91**, 325–334.
32 S. P. Lees-Miller, K. Sakaguchi, S. J. Ullrich, E. Appella and C. W. Anderson, *Mol. Cell. Biol.*, 1992, **12**, 5041–5049.
33 F. S. Shaheen, P. Znojek, A. Fisher, M. Webster, R. Plummer, L. Gaughan, G. C. M. Smith, H. Y. Leung, N. J. Curtin and C. N. Robson, *PLoS One*, 2011, **6**, e20311.
34 R. J. Flassig and K. Sundmacher, *Bioinformatics*, 2012, **28**, 3089–3096.
35 D. Davidson, Y. Coulombe, V. Martinez-Marignac, L. Amrein, J. Grenier, K. Hodkinson, J.-Y. Masson, R. Aloyz and L. Panasci, *Invest. New Drugs*, 2012, **30**, 1248–1256.

Supplementary Information

Experimental design, validation and computational modeling uncover DNA damage sensing by DNA-PK and ATM

Robert J Flassig*[1], Gunter Maubach[2], Christian Träger[2], Kai Sundmacher[1,3] and Michael Naumann[2]

[1]Max Planck Institute for Dynamics of Complex Technical Systems, Magdeburg, Germany
[2]Institute of Experimental Internal Medicine, Magdeburg, Germany
[3]Process Systems Engineering Group, Otto von Guericke University, Magdeburg, Germany

April 23, 2014

Contents

*flassig@mpi-magdeburg.mpg.de

1 Data Processing

The provided data constitute quantitative time-resolved immunoblotting data of γH2AX (including replicates) and active p53 at different experimental conditions. The raw data were quantified with ImageJ (Schneider et al., 2012) to yield grey level intensities. The measured grey levels $y_{ij}(t)$ at time t can be related to the amount of antibodies $a_{ij}(t)$ (lumping first and secondary antibody effects) as

$$y_{ij}(t) = \beta_{0i} + \beta_{1i} a_{ij}(t), \tag{1}$$

where i represents the experimental run effects via β_{0i} background, and exposure β_{1i}. Index j represents experimental conditions (e.g. varying irradiation dose). The amount of antibodies can be related to the amount of proteins in a similar way as

$$a_{ij}(t) = \alpha_0 + \alpha_1 p_{ij}(t), \tag{2}$$

whereas α_0 can be interpreted as unspecific binding effects and α_1 protein specific binding efficiency. The total protein amount in each lane $p_{ij}(t)$ is further affected by the loading i (loading effects, which belongs to experimental run effects) and the treatment j. In this form, lanes across one blot cannot be compared owing loading effects, let alone across different gels owing exposure, background, gel specific effects (e.g. transfer efficiency). Therefore, in order to allow (i) proper averaging over replicates as well as (ii) comparison amongst different experimental treatments, we have to normalize the quantified fluorescence levels. In the first step, different gels can be compared by normalizing the signals to a reference. Here we use the first time point of each signal. We then have

$$y_{ij}^{+}(t) = \frac{y_{ij}(t)}{y_{ij}(t=0)} = \frac{\alpha_0 + \alpha_1 p_{ij}(t)}{\alpha_0 + \alpha_1 p_{ij}(t=0)} \tag{3}$$

with removed backgrounds. The exposure term β_{1i} cancels out. Further, to account for loading effects we take the ratio

$$y_j^{\star} = \frac{y_{ij}^{+}(t)}{c_i^{+}(t)} = \frac{\alpha_0 + \alpha_1 p_{ij}(t)}{\xi_0 + \xi_1 c_i(t)} \frac{\xi_0 + \xi_1 c_i(t=0)}{\alpha_0 + \alpha_1 p_{ij}(t=0)}, \tag{4}$$

where $c_i(t)$ represents the loading control / house keeping protein. The house keeping protein is not affected by different experimental conditions, i.e. index j is not present. In this way, we have reduced variations due to experimental parameter variations indexed with i, i.e. effects due to variations in between experimental runs. Equation (4) can be related to a simulated, average, relative protein amount $p_{j_{\text{sim}}(t)}$ via

$$y_{j_{\text{sim}}}^{\star} = \frac{b_0 + b_1 p_{j_{\text{sim}}}(t)}{b_0 + b_1 p_{j_{\text{sim}}}(t=0)}, \tag{5}$$

where b_0 represents an offset and b_1 a scaling parameter.

Noise modeling: As has been shown by Kreutz et al. (2007) that experimental noise is best captured with a log-normal model. Therefore, data in the form of Eq. (4) as well as simulated response Eq. (5) are log-transformed. The final processed response data as well as the response model read

$$y_j = \log\left(\frac{y_j^+(t)}{c^+(t)}\right) \tag{6}$$

$$y_{j_{\text{sim}}} = \log\left(\frac{b_0 + b_1 p_{j_{\text{sim}}}(t)}{b_0 + b_1 p_{j_{\text{sim}}}(t=0)}\right). \tag{7}$$

Since we are modeling activation states of proteins upon stimulation, it is reasonable to assume $p_{j_{\text{sim}}}(t=0) = 0$ for activate states of each protein p under zero-stimulation condition. Then, Eq. 7 further simplifies to

$$y_{j_{\text{sim}}} = \log\left(1 + \text{scale}_p p_{j_{\text{sim}}}(t)\right), \tag{8}$$

with protein associated scaling parameter $\text{scale}_p = b_1/b_0$. This expression is used to relate measured signals of γH2AX and p53-P in processed form, Eq. (6), to the simulated ones, Eq. (8).

Before parameter estimation, we performed a balanced two-way ANOVA (along immunoblot gels and time-points) on the processed data to identify replicates in the data sets that differed significantly from the others at a confidence level of 95%. These data sets were identified and removed from the data. In the case of γH2AX the data variance was obtained from the sample variance. For p53-P, no replicates at the two different experimental conditions have been obtained. Therefore, the order of the variance of p53-P was estimated from the variance of the initial data.

2 Modeling Approach

2.1 Dynamic Model structure

The dynamics of the DNA damage response is modeled via ordinary differential equations. The dynamics of the internal states $\mathbf{x}(t, \mathbf{u}(t), \boldsymbol{\theta}_x) \in \mathbb{A}_{\mathbf{x}} \subset \mathbb{R}^{n_x}$, represent relative protein concentrations (relative, since the data do not allow to set an absolute scale) and is determined by the solution of an initial value problem of the form

$$\frac{\mathrm{d}}{\mathrm{d}t}\mathbf{x}(t) = \mathbf{f}(\mathbf{x}(t), \mathbf{u}(t), \boldsymbol{\theta}_{\mathbf{x}}) \tag{9}$$

with initial system states $\mathbf{x}(t_0) = \mathbf{x}_0$ and right hand side function $\mathbf{f}(\mathbf{x}(t), \mathbf{u}(t), \boldsymbol{\theta}_{\mathbf{x}})$ describing biologic interaction mechanisms, which depends on the system states $\mathbf{x}(t)$, (multiple) inputs $\mathbf{u}(t)$ (=stimulus), and kinetic parameter set $\boldsymbol{\theta}_{\mathbf{x}}$. The readout variables are determined by

$$\mathbf{y}_{\text{sim}}(t, \boldsymbol{\theta}) = \mathbf{g}(\mathbf{x}(t, \boldsymbol{\theta}_{\mathbf{x}}), \boldsymbol{\theta}_{\mathbf{y}}), \tag{10}$$

where the function $\mathbf{g}$ relates the internal system states to the readouts of the experiment with corresponding readout parameters $\boldsymbol{\theta}_{\mathbf{y}}$, which together with dynamic parameters and initial conditions are merged into the model parameter vector $\boldsymbol{\theta} = [\boldsymbol{\theta}_{\mathbf{x}}, \boldsymbol{\theta}_{\mathbf{y}}]^{\mathrm{T}}$, with redefined dynamic parameter vector $\boldsymbol{\theta}_{\mathbf{x}} \equiv [\boldsymbol{\theta}_{\mathbf{x}}, \mathbf{x}_0]^{\mathrm{T}}$. The readout function is defined by Eq. (8).

2.2 Modeling γH2AX activation upon genotoxic stress

Most of the interaction structure of the models has been constructed from available knowledge in the literature. The resulting topology is represented in Fig. 1. Ionizing radiation (IR) at a certain dose rate generates initial DSB (DDNA1) in a dose-dependent manner. Upon DSBs, cells trigger initial damage sensing and either use cNHEJ (fast) or HR/aNHEJ (slow) repair pathways. In detail, the damage signaling starts via the recognition of DDNA1 by Ku7080, its association to the damage site (RC11) and formation of the DNA-PK$_{\mathrm{cs}}$ complex (RC12). The catalytic subunit of DNA-PK$_{\mathrm{cs}}$ is then either phosphorylated by activated ATM or via autophosphorylation by DNA-PK$_{\mathrm{cs}}$ on the T2609 cluster, to initiate the NHEJ pathway (Chen et al., 2007). Here, we assume a two-step process as has been suggested by (Cucinotta et al., 2008). In parallel, the DSB can also be recognized by the MRN complex Mre11-Rad50-Nbs1, which can co-localize to the damage site to promote ATM activation, upon which ATM becomes autophosphorylated at Ser1981. This is modeled as a one step process as in (Mouri et al., 2009). One of the most important downstream targets of ATM during DDR is the tumor suppressor p53. Phosphorylation of p53 at Ser15 by ATM promotes its release from MDM2 and concomitants its activation (Canman et al., 1998; Shieh et al., 1997). Activation of p53 by DNA-PK$_{\mathrm{cs}}$ has also been described in the literature (Lees-Miller et al., 1992). However, DNA-PK-/- MEFs show normal p53 activation (Jimenez et al., 1999). We also did not find any evidence for a DNA-PK contribution, because the inhibition of DNA-PK$_{\mathrm{cs}}$ did not hamper the p53 phosphorylation (main document Fig. 2e). Therefore, we implemented the p53 activation as an ATM-dependent process only.
Failure to repair DSB via cNHEJ potentially releases DNA-PK$_{\mathrm{cs}}$ complexes and allows HR/aNHEJ repair proteins to access the damage site (Neal and Meek, 2011). These two major repair pathways split thus the initial DSB pool (DDNA1) into DDNA1 and DDNA2, whereas DDNA2 represents complex DSBs processed by HR/aNHEJ pathways. We model this branching from cNHEJ to HR/aNHEJ with a reaction triggered by active ATM. This is a reasonable assumption, since active ATM is required for HR/aNHEJ pathway activity (Koecher et al., 2012; Morrison et al., 2000). The detailed mechanisms that control the contribution of cNHEJ and HR/aNHEJ is not fully understood (Brandsma and Gent, 2012). We have generated four alternative models, which describe different mechanism of dynamic interaction of ATM, DNA-PK$_{\mathrm{cs}}$ and γH2AX including the branching into cNHEJ and HR/aNHEJ repair pathways (see Fig. 1). Model complexity has been reduced to the necessary interaction steps in view of the modeling aim, i.e. investigating the contribution of ATM and DNA-PK$_{\mathrm{cs}}$ to γH2AX activation on a dynamic basis. Proteins of large abundance in the cell have been assumed to be constant over the signaling time. In models A1 and A2, active ATM triggers the switch

to HR/aNHEJ before DDNA2, whereas in B1 and B2 the active ATM triggers after DDNA2. In A1 and B1 the active ATM as a trigger is modulated by the number of total DSBs, which is not the case in A2 and B2. These variants hypotethize, whether higher doses tend to induce more complex DSBs, which in turn need to be signaled to HR/aNHEJ. Since the initial signaling is restricted to the cell nucleus, the model describes the dynamics within the nucleus only.
From a pure signaling point of view, Ku7080 and MRN represent DSB signal sensors, whereas DNA-PK_{cs} and ATM (also ATR) DSB signal transducers. Similar to DNA-PK_{cs} in cNHEJ repair, Rad52 is a DSB repair mediator in HR. Repair by cNHEJ was modeled as a one-step process (RC12 to RDNA1). HR/aNHEJ have longer processing time, therefore a two-step process was assumed comprising association of Rad52 to DDNA2 and subsequent repair (RDNA2). Activation of γH2AX is mediated by active DNA-PK_{cs} in single or double phosphorylated form or active ATM. Since the model is focusing on γH2AX activation, which reflects the early phase in damage signaling, dephosphorylation of γH2AX is modeled as a simple first order reaction, independent of the repair process. The same holds for active ATM de-phosphorylation. All inactive forms of Ku7080, MRN, DNA-PK_{cs}, ATM, Rad52 and $H2AX_{tot}$ are highly abundant. Their respective amounts in the cell are therefore assumed to be constant, which is especially valid when looking at the initial transient signaling. As a consequence, the hypothesized stabilization of ATM by DNA-PK_{cs} (in inactive form) is indirectly accounted for (Shrivastav et al., 2009). After OED I was performed, we added p53 to the models to better dissect individual contributions of DNA-PK_{cs} and ATM in combination with inhibitions experiments.

2.3 Model Equations

The model equations are scaled to the total concentration of $[\text{Ku7080}]_{\text{tot}}$ to make use of the intrinsic scale invariance of ODE in dimensional form to improve parameter estimation in terms of efficiency, see for instance supplement of Bachmann et al. (2011). Therefore, brackets - usually indicating a protein in concentration units - have been dropped, as the states of the ODE then represent relative concentration levels and are

thus dimensionless.

initially damaged DNA: $$\frac{\mathrm{d}}{\mathrm{dt}}\mathrm{DDNA1} = R_1 - R_2 \tag{11}$$

complex {Ku7080:DDNA1}: $$\frac{\mathrm{d}}{\mathrm{dt}}\mathrm{RC11} = R_2 - R_3 \tag{12}$$

complex {DNA-PK$_{cs}$:RC11}: $$\frac{\mathrm{d}}{\mathrm{dt}}\mathrm{RC12} = R_3 - R_4 - R_{6\mathcal{M}} \tag{13}$$

1st phosphorylation step RC12: $$\frac{\mathrm{d}}{\mathrm{dt}}\mathrm{RC12}^p = R_4 - R_5 \tag{14}$$

2nd phosphorylation step RC12: $$\frac{\mathrm{d}}{\mathrm{dt}}\mathrm{RC12}^{pp} = R_5 - R_7 \tag{15}$$

complex damaged DNA: $$\frac{\mathrm{d}}{\mathrm{dt}}\mathrm{DDNA2} = R_{6\mathcal{M}} - R_{9\mathcal{M}} \tag{16}$$

complex {MRN:DDNA1}: $$\frac{\mathrm{d}}{\mathrm{dt}}\mathrm{RC20} = R_{10} - R_{11} \tag{17}$$

complex {ATM:RC20}: $$\frac{\mathrm{d}}{\mathrm{dt}}\mathrm{RC21} = R_{11} - R_{12} \tag{18}$$

double phosphorylated ATM: $$\frac{\mathrm{d}}{\mathrm{dt}}\mathrm{RC21}^{pp} = R_{12} - R_{15} \tag{19}$$

complex repair step: $$\frac{\mathrm{d}}{\mathrm{dt}}\mathrm{RC22}^{pp} = R_{9\mathcal{M}} - R_8 \tag{20}$$

repaired DNA: $$\frac{\mathrm{d}}{\mathrm{dt}}\mathrm{RDNA1} = R_7 \tag{21}$$

repaired DNA: $$\frac{\mathrm{d}}{\mathrm{dt}}\mathrm{RDNA2} = R_8 \tag{22}$$

γH2AX: $$\frac{\mathrm{d}}{\mathrm{dt}}\gamma = R_{13} - R_{14} \tag{23}$$

total damaged DNA: $$\frac{\mathrm{d}}{\mathrm{dt}}\mathrm{tDSB} = R_1 \tag{24}$$

phosphorylated p53: $$\frac{\mathrm{d}}{\mathrm{dt}}\mathrm{p53}^p = R_{16} - R_{17} \tag{25}$$

Corresponding rates

$$R_1 = \alpha_0 \frac{\mathrm{d}D}{\mathrm{dt}} u(t) \tag{26}$$
$$R_2 = \alpha_{11}\mathrm{DDNA1} \tag{27}$$
$$R_3 = \alpha_{12}\mathrm{RC11} \tag{28}$$
$$R_4 = \alpha_{13}\mathrm{RC12} \tag{29}$$
$$R_5 = \alpha_{141}(1 + \alpha_{142}\mathrm{RC21}^{pp})\mathrm{RC12}^{p} \tag{30}$$
$$R_{6A1} = \alpha_{15}\mathrm{tDSB}\,\mathrm{RC21}^{pp}\mathrm{RC12} \tag{31}$$
$$R_{6B1} = \alpha_{15}\mathrm{tDSB}\,\mathrm{RC12} \tag{32}$$
$$R_{6A2} = \alpha_{15}\mathrm{RC21}^{pp}\mathrm{RC12} \tag{33}$$
$$R_{6B2} = \alpha_{15}\mathrm{RC12} \tag{34}$$
$$R_7 = \delta_{16}\mathrm{RC12}^{pp} \tag{35}$$
$$R_8 = \delta_{16}\mathrm{RC22}^{pp} \tag{36}$$
$$R_{9A12} = \alpha_{17}\mathrm{DDNA2} \tag{37}$$
$$R_{9B12} = \alpha_{17}\mathrm{RC21}^{pp}\mathrm{DDNA2} \tag{38}$$
$$R_{10} = \alpha_{21}\mathrm{DDNA1} \tag{39}$$
$$R_{11} = \alpha_{22}\mathrm{RC20} \tag{40}$$
$$R_{12} = \alpha_{231}(1 + \alpha_{232}\mathrm{RC21}^{pp})\mathrm{RC21}) \tag{41}$$
$$R_{13} = \frac{a_{25}(\mathrm{RC12}^{p} + \mathrm{RC12}^{pp} + \mathrm{RC21}^{pp})}{a_{25M} + \mathrm{RC12}^{p} + \mathrm{RC12}^{pp} + \mathrm{RC21}^{pp}}(\xi - \gamma) \tag{42}$$
$$R_{14} = \alpha_{26}\gamma \tag{43}$$
$$R_{15} = \alpha_{23}\mathrm{RC21}^{pp} \tag{44}$$
$$R_{16} = \alpha_{24}\mathrm{RC21}^{pp} \tag{45}$$
$$R_{17} = \alpha_{25}\mathrm{p53}^{p}. \tag{46}$$

Here, $u(t)$ represents the stimulus in form of a switching function, i.e. if the system is irradiated at dose rate $\frac{\mathrm{d}D}{\mathrm{dt}}$, $u(t) = 1$. If the system is not irradiated, $u(t) = 0$.

2.4 Parameter Inference

The parameters are estimated based on the maximum likelihood principle. Owing data processing, log-transform, noise model and ANOVA analysis (see Sec. 1), standard conditions can be assumed to hold. In fact, we verify this assumption after obtaining a fit by using Anderson-Darling statistics (see Tab. 1 in the main document). By this we also test model adequacy. We thus minimize the residual sum of squares

$$\chi^2(\boldsymbol{\theta}) = \sum_{i=1}^{n} \frac{\left(Y_i - y_{i_{\mathrm{sim}}}(\boldsymbol{\theta})\right)^2}{\sigma_Y^2} = \text{const.} - 2l_(y_{i_{\mathrm{sim}}}(\boldsymbol{\theta})) \tag{47}$$

to yield a maximum likelihood estimate, where $l(y_{i_{\text{sim}}}(\boldsymbol{\theta}))$ represent the log-likelihood function, and summation is performed over all experimental data. Only the last term depends on $\boldsymbol{\theta}$. Therefore minimizing $\chi^2(\boldsymbol{\theta})$ with respect to $\boldsymbol{\theta}$ is equivalent to maximizing $l(\boldsymbol{\theta})$. The variance σ_Y^2 is estimated for each measured response and time point using the replicates in the data sets.
The objective function Eq. (47) itself was minimized using a hybrid optimization strategy, combining a genetic algorithm and interior-point/active-set optimization, which are implemented in MATLAB, to find a nearly global optimum. The models were also implemented in MATLAB and solved using the CVODES solver from (Hindmarsh et al., 2005). Rate constants and scaling parameters are positive and typically distributed on a logarithmic scale (Gutenkunst et al., 2007; Limpert et al., 2001). Therefore, the parameter estimation was performed on a logarithmic scale. Further, possible realizations of the kinetic parameters were constrained to the interval $[10^{-2} \dots 10^{+2}]$, whereas upper bounds of scaling parameters have been adjusted up to 10^4. Overall, 19 kinetic parameters and 8 scaling parameters per model were estimated. As already mention above, initial conditions of the proteins where assumed to be zero, reflecting zero activity of the unperturbed states. The inactive proteins Ku7080, MRN, DNA-PK$_{\text{cs}}$, ATM and H2AX have large abundance, which allowed to reduce the number of parameters by assuming a constant supply of inactive to active protein forms. In the case of γH2AX, the conservation relation

$$H2AX_{\text{tot}} = H2AX + \gamma H2AX \tag{48}$$

has been used to simplify the back reaction. The final parameter for the final identified model A2 are given in the Supplementary Table 1 in logarithmic representation. The lower and upper 95% point-wise confidence bounds are derived from the profile likelihood (see Sec. 2.5). Bounds with $\pm\infty$ indicate that the profile likelihood did not reach the critical value for significance. Notice that we have restricted the optimization effort for each model by constraining the parameter bounds on a range of 4 orders of magnitude in logarithmic space.

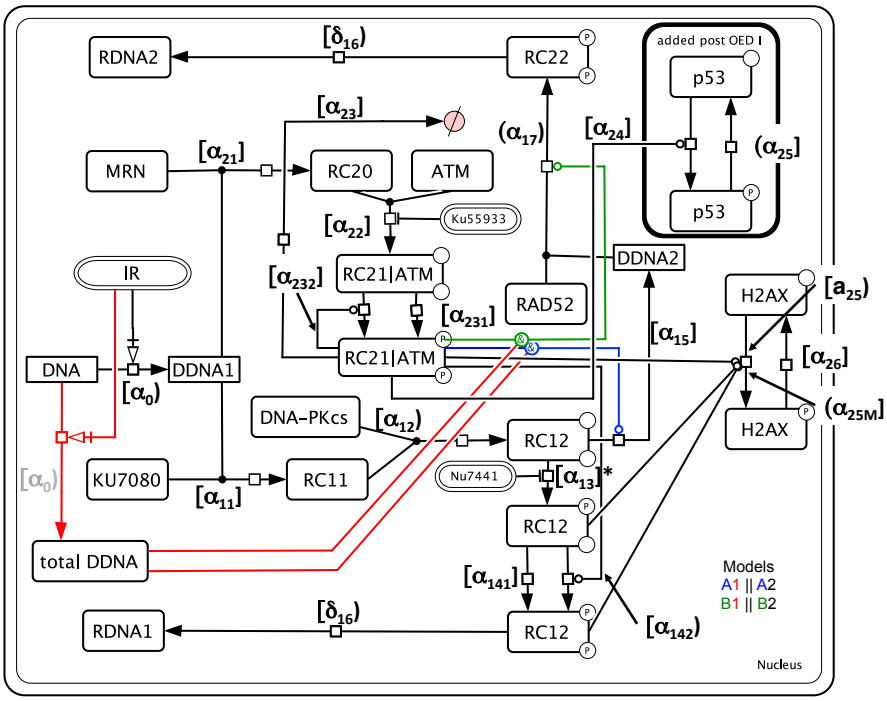

Supplementary Figure 1: The model structure is shown as an interaction graph, including 4 different versions of active ATM processing. Interactions are modeled via state transitions (arrows with squares), enzyme catalysis (lines with circles) and complex formation (joined lines). Stimulus and inhibitors have round-edge boxes. Activation of DNA-PK$_{cs}$, ATM and subsequent γH2AX is modeled by two parallel pathways. The contribution to DNA DSB repair due to DNA-PK$_{cs}$ or ATM signaling is modeled via branching of the damaged DNA pool resulting into a split of the initial damaged DSB DNA (DDNA1) into DDNA1 and DDNA2. Four mechanisms have been considered for branching (A1, A2, B1, B2). A and B refer to the location of the catalytic activity of ATM, which is used to model the availability of HR/aNHEJ proteins, as theses depend on ATM activation. Index 1 and 2 refer to the kinetic law used. For models A/B in variant 1 branching to DDNA2 is catalyzed by the total amount of damaged DNA, which models the shift to HR/aNHEJ due to increased numbers of complex DSB at higher doses. Model variants A/B with index 2 do not use the total amount of damaged DNA. P53 has been added after OED I, as this was monitored during titration. Reaction parameters are also indicated, including the identifiability status (for model A2 only): parameter p is $[p]$ identifiable, $[p]^*$ identifiable, exceeding the upper optimization bound, $[p)$ non-identifiable upper limit, $(p]$ non-identifiable lower limit, (p) structurally non-identifiable.

Supplementary Table 1: Final parameter set for model A2 and profile likelihood base lower and upper (LB,UB) 95% point-wise confidence bounds in log-space. Scaling parameters are represented as $\xi = \frac{[H2AX_{\text{tot}}]}{[\text{Ku7080}_{\text{tot}}]}$ and s_i and are in principle non-identifiable owing relative measurement data.

Parameter	Units	LB	$\log_{10}(\theta)$	UB
$\alpha_0 = \frac{a_0}{[\text{Ku7080}_{\text{tot}}]}$	Gy^{-1}	1.2024	1.7262	∞
$\alpha_{11} = a_{11}[\text{Ku7080}_{\text{tot}}]$	min^{-1}	-1.6041	-1.4588	-1.3195
$\alpha_{12} = a_{12}[\text{Ku7080}_{\text{tot}}]$	min^{-1}	-0.2517	1.5123	∞
$\alpha_{13} = a_{13}[\text{Ku7080}_{\text{tot}}]$	min^{-1}	1.8086	2.0000	∞
$\alpha_{141} = a_{141}[\text{Ku7080}_{\text{tot}}]$	min^{-1}	-0.9869	-0.5246	-0.2279
$\alpha_{142} = \frac{a_{142}}{a_{141}}[\text{Ku7080}_{\text{tot}}]$	1	1.2977	1.7342	∞
$\alpha_{15} = a_{15}[\text{Ku7080}_{\text{tot}}]$	min^{-1}	-0.7768	-0.2492	0.1913
$\delta_{16} = d_{16}[\text{Ku7080}_{\text{tot}}]$	1	1.4718	1.9601	∞
$\alpha_{17} = a_{17}[\text{Ku7080}_{\text{tot}}]$	min^{-1}	$-\infty$	0.5089	∞
$\alpha_{21} = a_{21}[\text{Ku7080}_{\text{tot}}]$	min^{-1}	-0.7612	-0.4635	0.2067
$\alpha_{22} = a_{22}[\text{Ku7080}_{\text{tot}}]$	min^{-1}	-0.9253	-0.6773	-0.3882
$\alpha_{231} = a_{231}[\text{Ku7080}_{\text{tot}}]$	min^{-1}	-1.7834	-0.3972	0.2888
$\alpha_{232} = a_{232}[\text{Ku7080}_{\text{tot}}]$	min^{-1}	0.7257	1.2354	1.5524
a_{25}	min^{-1}	0.2562	1.355	∞
$\alpha_{25M} = a_{25M}[\text{Ku7080}_{\text{tot}}]$	M^2	$-\infty$	-2	-1.8033
$\alpha_{26} = a_{26}[\text{Ku7080}_{\text{tot}}]$	min^{-1}	-0.1947	0.6083	1.0618
$\alpha_{23} = a_{23}[\text{Ku7080}_{\text{tot}}]$	min^{-1}	-0.0538	0.2526	1.1834
$\alpha_{24} = a_{24}[\text{Ku7080}_{\text{tot}}]$	min^{-1}	-1.6565	-1.2240	-0.8093
$\alpha_{25} = a_{25}[\text{Ku7080}_{\text{tot}}]$	min^{-1}	$-\infty$	-1.7197	-0.8152
$\xi = \frac{[H2AX_{\text{tot}}]}{[\text{Ku7080}_{\text{tot}}]}$	1	-	-0.6832	-
s_0	1	-	2.7705	-
s_1	1	-	2.4559	-
s_2	1	-	2.6787	-
s_3	1	-	2.7727	-
s_4	1	-	3.0366	-
s_5	1	-	1.9483	-
s_6	1	-	-1.0169	-

2.5 Profile Likelihood Analysis

For model A2, we calculated the profile likelihood χ^2_{PL} as for instance described in (Raue et al., 2009), which we have implemented in MATLAB in combination with the fast CVODES ODE integration package (Hindmarsh et al., 2005). Absolute and relative tolerances have been set to 10^{-7} and 10^{-6}, respectively. The MATLAB implementation of the profile likelihood algorithm has been parallelized and is based on a template from the first author of (Raue et al., 2009). In Figures 2-20, we show the profile likelihoods for the kinetic parameters and the parameter dependencies in terms of relative parameter change for each kinetic parameter, when moving along the profile likelihood of each specific parameter in log-space. The relative parameter change of a parameter θ_m for in- or decreasing parameter θ_n from its maximum likelihood estimate and $n \neq m$ is defined as

$$\delta\theta_{i,m} = \frac{\theta_{i,m} - \theta_m}{\theta_m}, \tag{49}$$

with index i representing a position along the profile likelihood of θ_n and θ_m being the maximum likelihood estimate of model A2, $m \in \{1, ..., 19\} \backslash n$.
As a rough interpretation guide, flat profile likelihoods indicate non-identifiable parameters, whereas profile likelihood that pass the critical $\chi^2_{\alpha=0.05,\mathrm{df}=1}$ value on both sides of the maximum-likelihood estimate of each parameter indicate an identifiable parameter. Profile likelihoods that hit the critical $\chi^2_{\alpha=0.05,\mathrm{df}=1}$ value (in the Figures indicated by the red line) only on one side indicate practically non-identifiable parameters. In this case, at least the lower or upper bound of the parameter are bounded. Since we have only relative data, $\xi = \frac{[H2AX_{\mathrm{tot}}]}{[\mathrm{Ku7080}_{\mathrm{tot}}]}$ and the readout scaling parameters are non-identifiable. This means, that the model cannot be used to predict absolute values of protein concentration. However, quantitative predictions regarding protein dynamics are possible. This is due to the fact, that the scaling parameters do no influence the right hand side of the ODE system. Like the authors of Bachmann et al. (2011), we thus treat scaling parameters as nuisance parameters.

Discussion on non-identifiable parameters:

Parameter α_0 has a non-identifiable upper bound for the given parameter estimation setup. The parameter represents the number of DNA double strand breaks per dose generated for a given dose rate. This means that the model structure has enough degrees of freedom to compensate higher but not too low DNA double strand breaks per dose rates for the given optimization setup. Thus, a minimal rate of DNA damage is needed to trigger the signaling. Compensation abilities by the model owing to limited information in the data is also apparent from the many parameter variations in terms of relative parameter change along the profile likelihood of α_0. The parameter can be interpreted as a damage impact scaling parameter setting the scale of the downstream parameters. The qualitative behavior of protein dynamics is thus not changed.

α_{12} represents the complex formation step between Ku7080 and DNA-PK$_{cs}$. According to the profile likelihood bounds, a minimal rate of complex formation is needed, whereas the upper bound is unconstrained. This means that complex formation may be arbitrary fast, thus this reaction step may be neglected (model reduction). However, we leave this step in the model, as it represents a verified interaction (Chan et al., 2002; Cui et al., 2005; Ferguson et al., 2000; Martin et al., 2005).

If α_{13} is increased above the upper optimization constraint, it then becomes identifiable. This means, that in principle the parameter is identifiable.

α_{142} describes the catalysis of the second phosphorylation step of DNA-PK$_{cs}$ by ATM and has an unconstrained upper bound. This means, that catalysis of ATM seems to be necessary, however several parameters can compensate increased catalytic activity of this reaction (see relative change of the parameters along the profile likelihood). For instance α_{141}, which represents the parallel reaction not catalyzed by ATM, anti-correlates with α_{142}. Note that α_{142} is identifiable owing to the data set where ATM is inhibited, which in turn makes the contribution of α_{142} negligible small and thus uncovers α_{141}.

δ_{16} is used to model the final repair step for both, cNHEJ and HR/aNHEJ. This parameter has a lower bound, ensuring a minimal turnover of $RC21^{pp}$, which is related to the measurement signal. Since the upper bound of δ_{16} is unconstrained, both repair steps can be arbitrarily fast in the model.

Parameter α_{17} represents the reaction from Rad52 to RC22. As no measurement information is provided for this specific step, this reaction is thus unconstrained for the given data. Note that the subsequent δ_{16} reaction has a lower bound, since it is also used in the DNA-PK$_{cs}$ part. In principle, this reaction can be withdrawn from the model to reduce model complexity.

α_{25M} and a_{25} are both related to the activation of γH2AX. Parameter a_{25} has an unconstrained upper bound, whereas α_{25M} is unconstrained on the lower bound. It can also be further reduced improving the overall fit.

Parameter α_{25} represents the degradation of p53-P and can in principle be arbitrarily fast.

In Fig. 21 we show a simulation along the profile likelihood for all model states for a 5 Gy pulse. We see that the states associated to non-identifiable parameters have larger uncertainty bands. Even though γH2AX has a noticeable uncertainty band, biphasic characteristics is however preserved and should still be observed experiments with suitable temporal resolution. Further, the small oscillatory part (visibile in the panels of ATM-p (RC21^{pp}) of Fig. 21; Fig. 3 A in the main document) and γH2AX signal) can be attributed to the feedback of ATM-p.

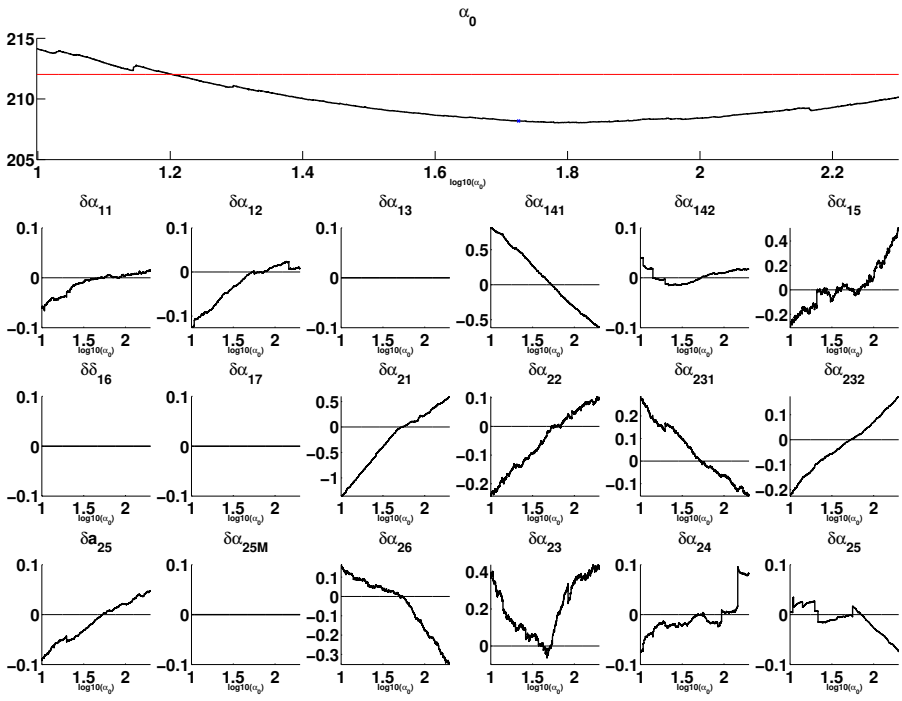

Supplementary Figure 2: Profile likelihood of model A2 for the specified kinetic parameter (upper panel, black line) and its dependencies on the remaining kinetic parameters in terms of relative change of each kinetic parameter in logspace (vertical axes of the small 3 x 6 subplots). The vertical axis in the upper panel indicates $\chi^2(\boldsymbol{\theta}_i)$, which is proportional to -2 times the profile likelihood value, whereas the horizontal axis represents the parameter value in logspace. The red line in the upper panel indicates the critical value for significance. The parameter value of the point estimate is indicated by a small blue cross in the upper panel.

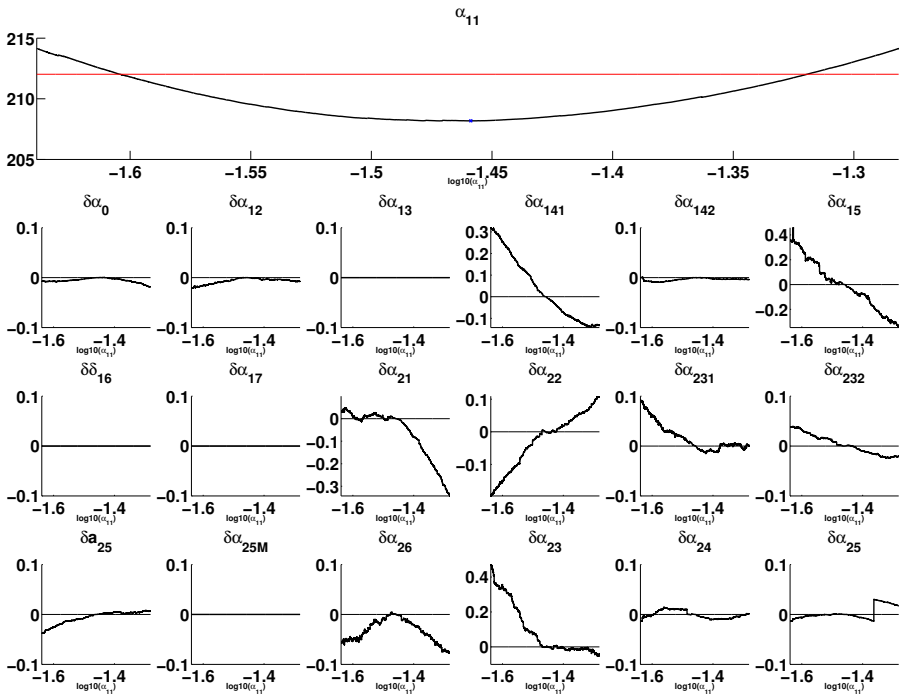

Supplementary Figure 3: Profile likelihood of model A2 for the specified kinetic parameter (upper panel, black line) and its dependencies on the remaining kinetic parameters in terms of relative change of each kinetic parameter in logspace (vertical axes of the small 3 x 6 subplots). The vertical axis in the upper panel indicates $\chi^2(\boldsymbol{\theta}_i)$, which is proportional to -2 times the profile likelihood value, whereas the horizontal axis represents the parameter value in logspace. The red line in the upper panel indicates the critical value for significance. The parameter value of the point estimate is indicated by a small blue cross in the upper panel.

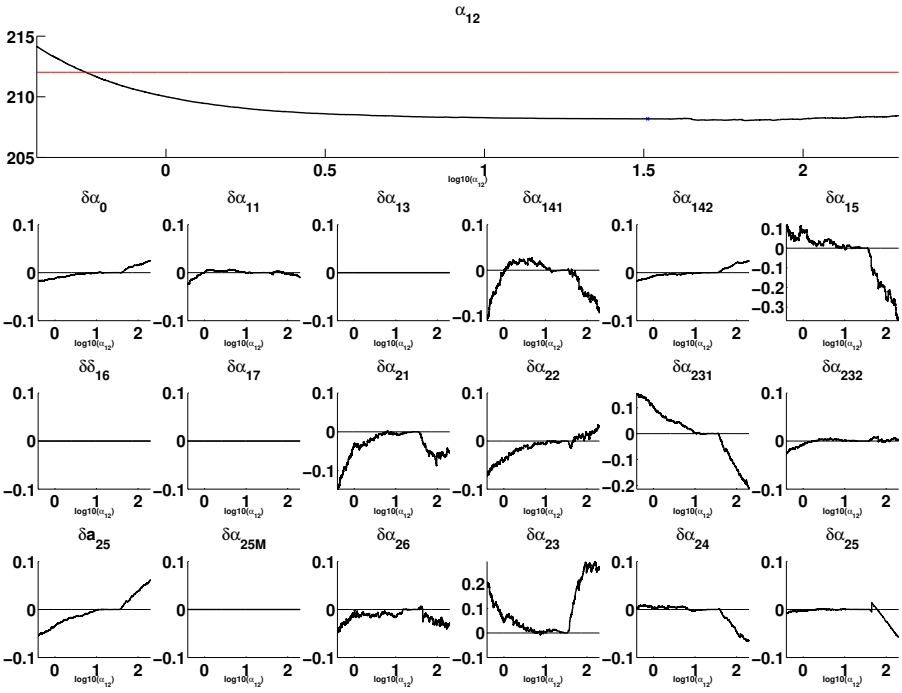

Supplementary Figure 4: Profile likelihood of model A2 for the specified kinetic parameter (upper panel, black line) and its dependencies on the remaining kinetic parameters in terms of relative change of each kinetic parameter in logspace (vertical axes of the small 3 x 6 subplots). The vertical axis in the upper panel indicates $\chi^2(\boldsymbol{\theta}_i)$, which is proportional to -2 times the profile likelihood value, whereas the horizontal axis represents the parameter value in logspace. The red line in the upper panel indicates the critical value for significance. The parameter value of the point estimate is indicated by a small blue cross in the upper panel.

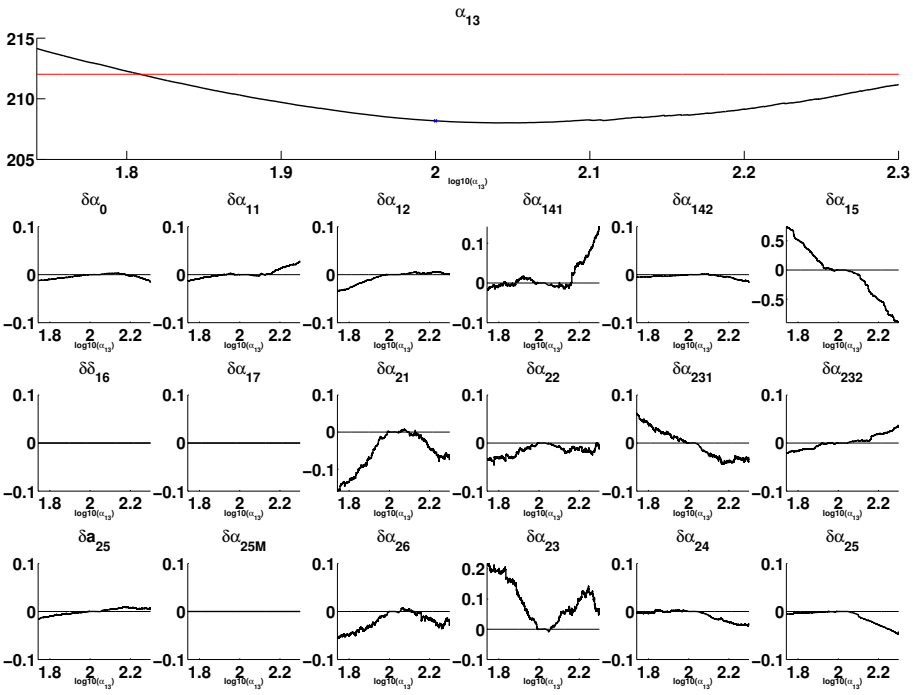

Supplementary Figure 5: Profile likelihood of model A2 for the specified kinetic parameter (upper panel, black line) and its dependencies on the remaining kinetic parameters in terms of relative change of each kinetic parameter in logspace (vertical axes of the small 3 x 6 subplots). The vertical axis in the upper panel indicates $\chi^2(\boldsymbol{\theta}_i)$, which is proportional to -2 times the profile likelihood value, whereas the horizontal axis represents the parameter value in logspace. The red line in the upper panel indicates the critical value for significance. The parameter value of the point estimate is indicated by a small blue cross in the upper panel.

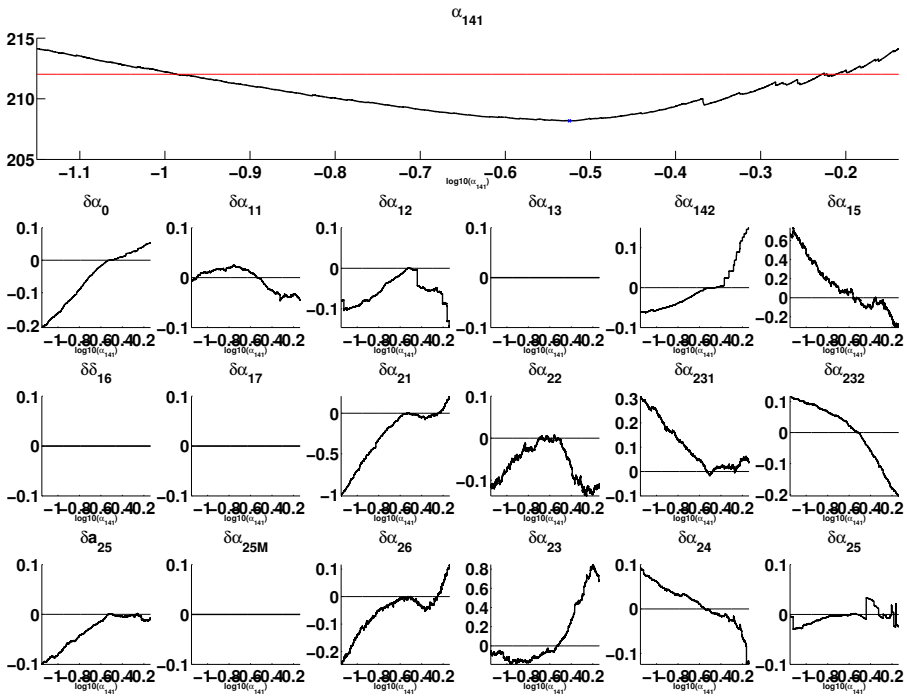

Supplementary Figure 6: Profile likelihood of model A2 for the specified kinetic parameter (upper panel, black line) and its dependencies on the remaining kinetic parameters in terms of relative change of each kinetic parameter in logspace (vertical axes of the small 3 x 6 subplots). The vertical axis in the upper panel indicates $\chi^2(\boldsymbol{\theta}_i)$, which is proportional to -2 times the profile likelihood value, whereas the horizontal axis represents the parameter value in logspace. The red line in the upper panel indicates the critical value for significance. The parameter value of the point estimate is indicated by a small blue cross in the upper panel.

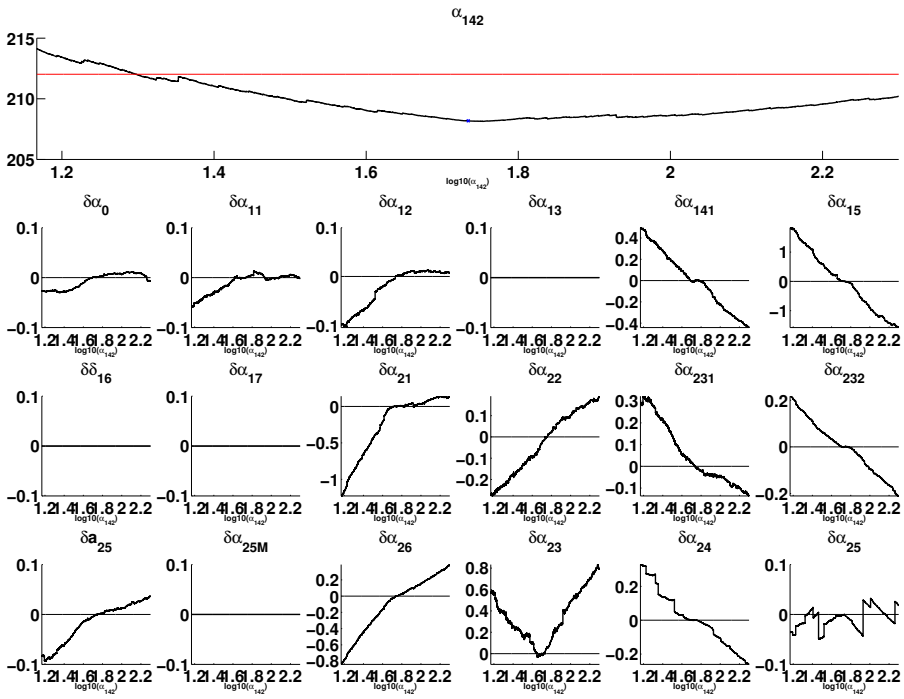

Supplementary Figure 7: Profile likelihood of model A2 for the specified kinetic parameter (upper panel, black line) and its dependencies on the remaining kinetic parameters in terms of relative change of each kinetic parameter in logspace (vertical axes of the small 3 x 6 subplots). The vertical axis in the upper panel indicates $\chi^2(\boldsymbol{\theta}_i)$, which is proportional to -2 times the profile likelihood value, whereas the horizontal axis represents the parameter value in logspace. The red line in the upper panel indicates the critical value for significance. The parameter value of the point estimate is indicated by a small blue cross in the upper panel.

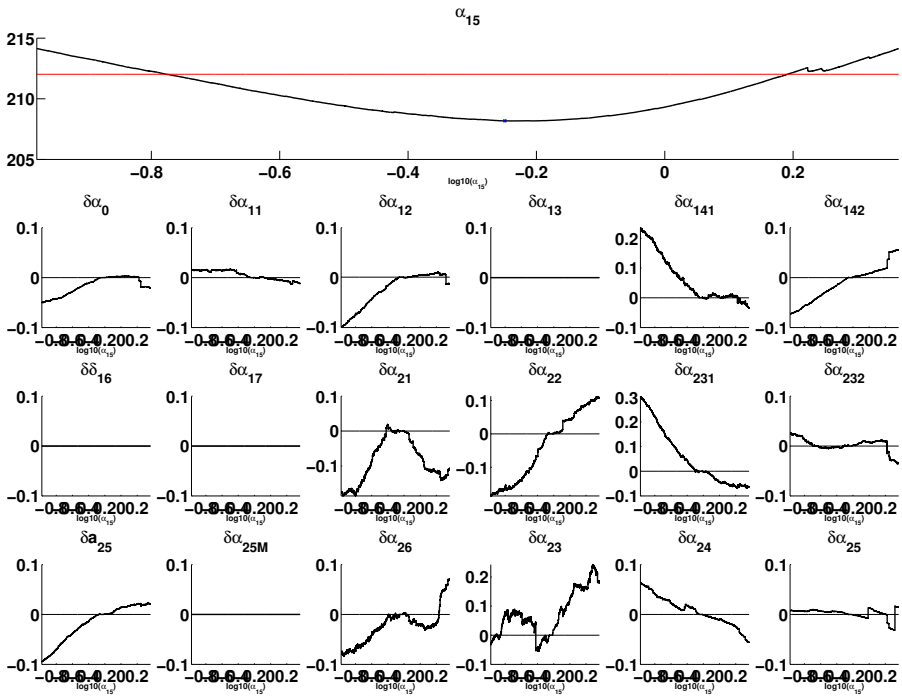

Supplementary Figure 8: Profile likelihood of model A2 for the specified kinetic parameter (upper panel, black line) and its dependencies on the remaining kinetic parameters in terms of relative change of each kinetic parameter in logspace (vertical axes of the small 3 x 6 subplots). The vertical axis in the upper panel indicates $\chi^2(\boldsymbol{\theta}_i)$, which is proportional to -2 times the profile likelihood value, whereas the horizontal axis represents the parameter value in logspace. The red line in the upper panel indicates the critical value for significance. The parameter value of the point estimate is indicated by a small blue cross in the upper panel.

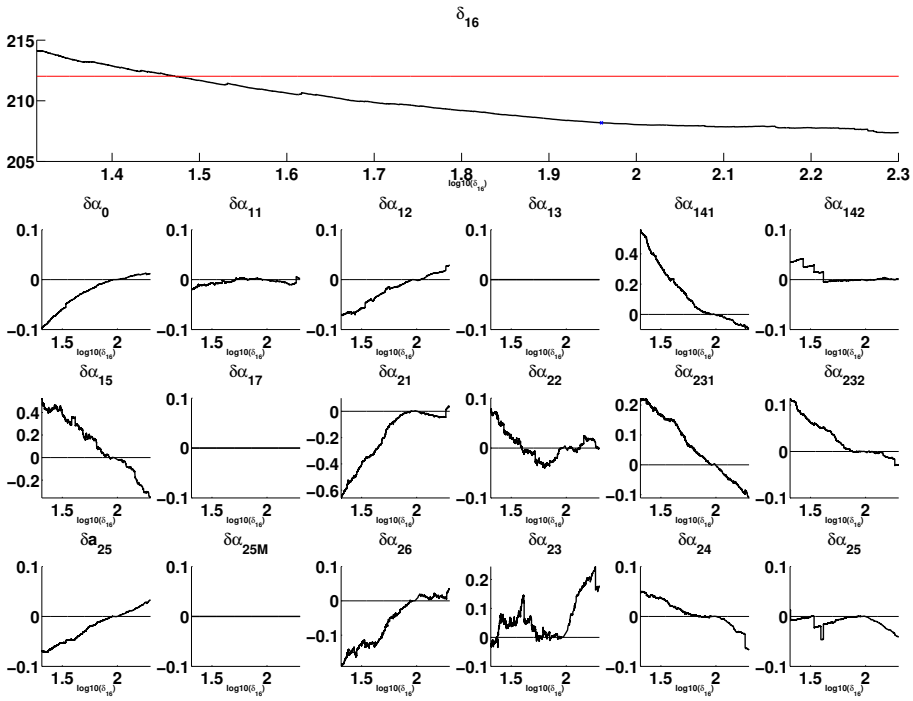

Supplementary Figure 9: Profile likelihood of model A2 for the specified kinetic parameter (upper panel, black line) and its dependencies on the remaining kinetic parameters in terms of relative change of each kinetic parameter in logspace (vertical axes of the small 3 x 6 subplots). The vertical axis in the upper panel indicates $\chi^2(\boldsymbol{\theta}_i)$, which is proportional to -2 times the profile likelihood value, whereas the horizontal axis represents the parameter value in logspace. The red line in the upper panel indicates the critical value for significance. The parameter value of the point estimate is indicated by a small blue cross in the upper panel.

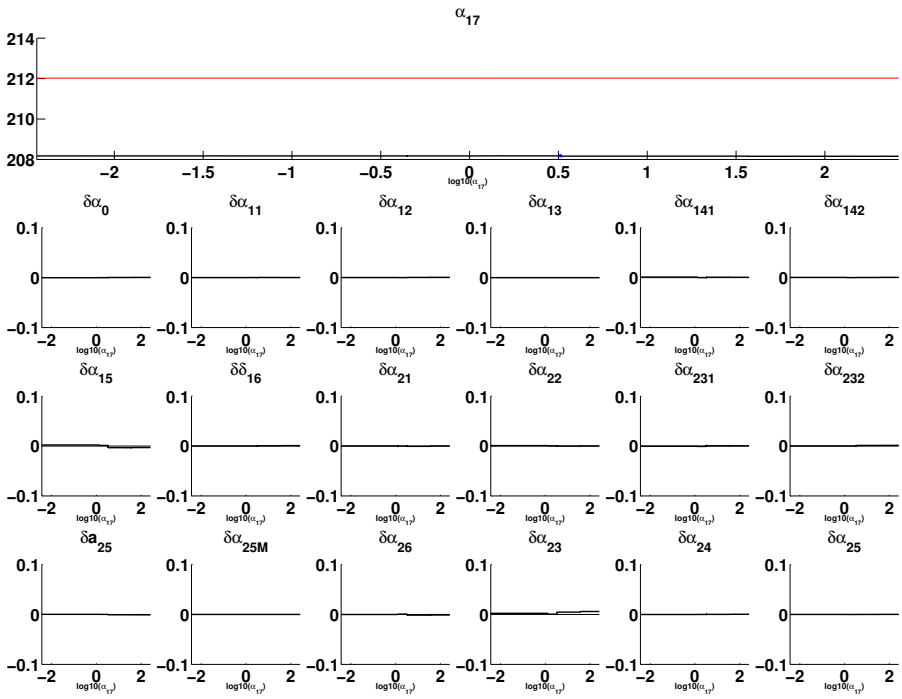

Supplementary Figure 10: Profile likelihood of model A2 for the specified kinetic parameter (upper panel, black line) and its dependencies on the remaining kinetic parameters in terms of relative change of each kinetic parameter in logspace (vertical axes of the small 3 x 6 subplots). The vertical axis in the upper panel indicates $\chi^2(\boldsymbol{\theta}_i)$, which is proportional to -2 times the profile likelihood value, whereas the horizontal axis represents the parameter value in logspace. The red line in the upper panel indicates the critical value for significance. The parameter value of the point estimate is indicated by a small blue cross in the upper panel.

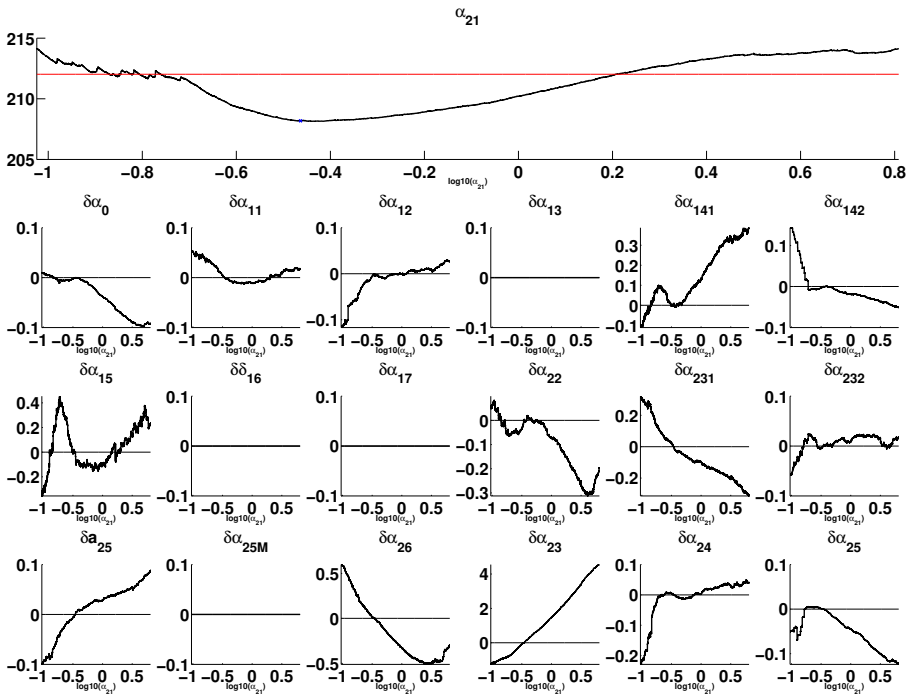

Supplementary Figure 11: Profile likelihood of model A2 for the specified kinetic parameter (upper panel, black line) and its dependencies on the remaining kinetic parameters in terms of relative change of each kinetic parameter in logspace (vertical axes of the small 3 x 6 subplots). The vertical axis in the upper panel indicates $\chi^2(\boldsymbol{\theta}_i)$, which is proportional to -2 times the profile likelihood value, whereas the horizontal axis represents the parameter value in logspace. The red line in the upper panel indicates the critical value for significance. The parameter value of the point estimate is indicated by a small blue cross in the upper panel.

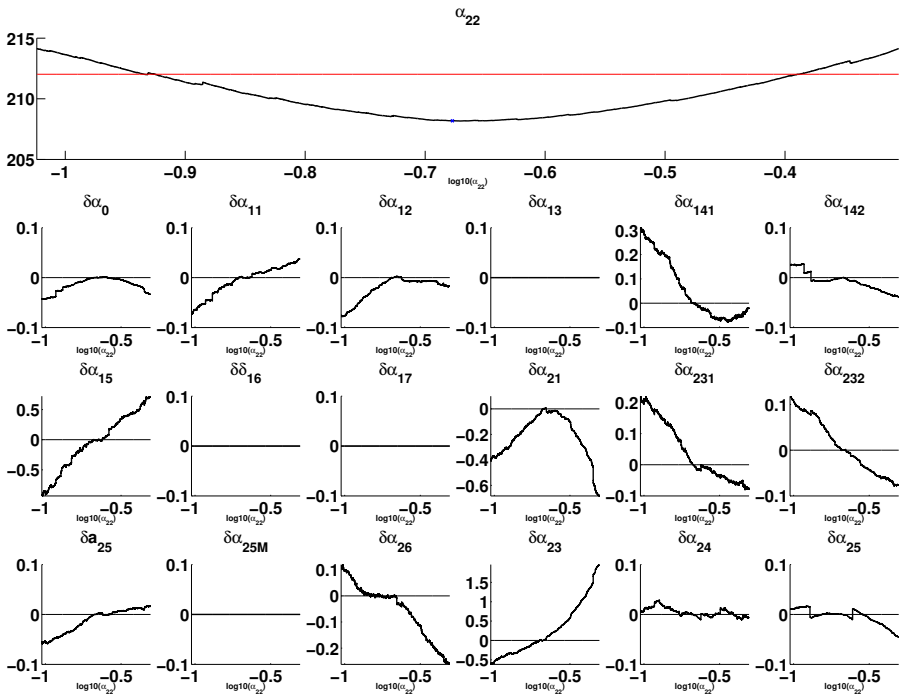

Supplementary Figure 12: Profile likelihood of model A2 for the specified kinetic parameter (upper panel, black line) and its dependencies on the remaining kinetic parameters in terms of relative change of each kinetic parameter in logspace (vertical axes of the small 3 x 6 subplots). The vertical axis in the upper panel indicates $\chi^2(\boldsymbol{\theta}_i)$, which is proportional to -2 times the profile likelihood value, whereas the horizontal axis represents the parameter value in logspace. The red line in the upper panel indicates the critical value for significance. The parameter value of the point estimate is indicated by a small blue cross in the upper panel.

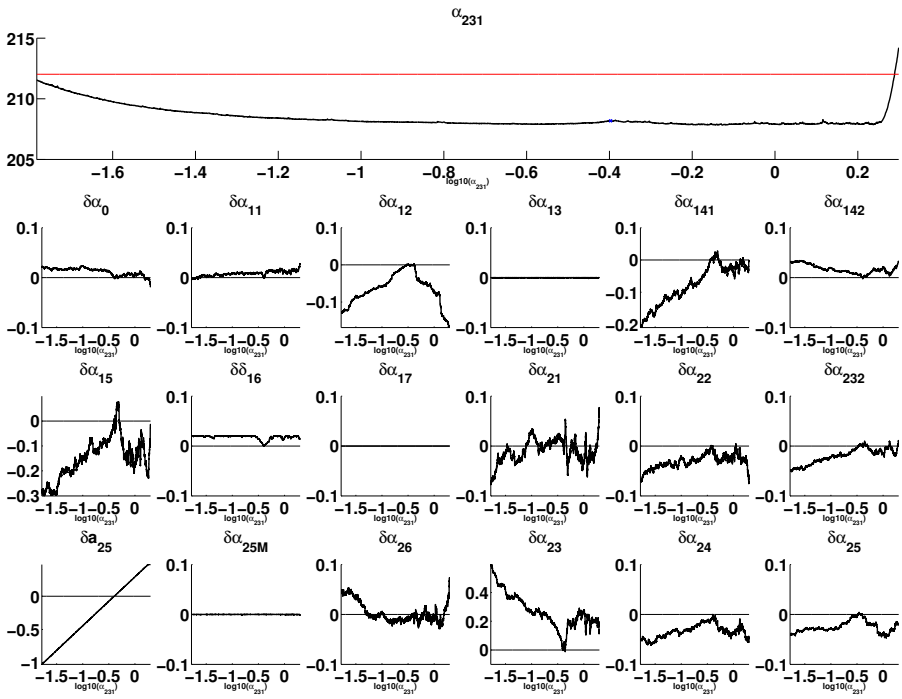

Supplementary Figure 13: Profile likelihood of model A2 for the specified kinetic parameter (upper panel, black line) and its dependencies on the remaining kinetic parameters in terms of relative change of each kinetic parameter in logspace (vertical axes of the small 3 x 6 subplots). The vertical axis in the upper panel indicates $\chi^2(\boldsymbol{\theta}_i)$, which is proportional to -2 times the profile likelihood value, whereas the horizontal axis represents the parameter value in logspace. The red line in the upper panel indicates the critical value for significance. The parameter value of the point estimate is indicated by a small blue cross in the upper panel.

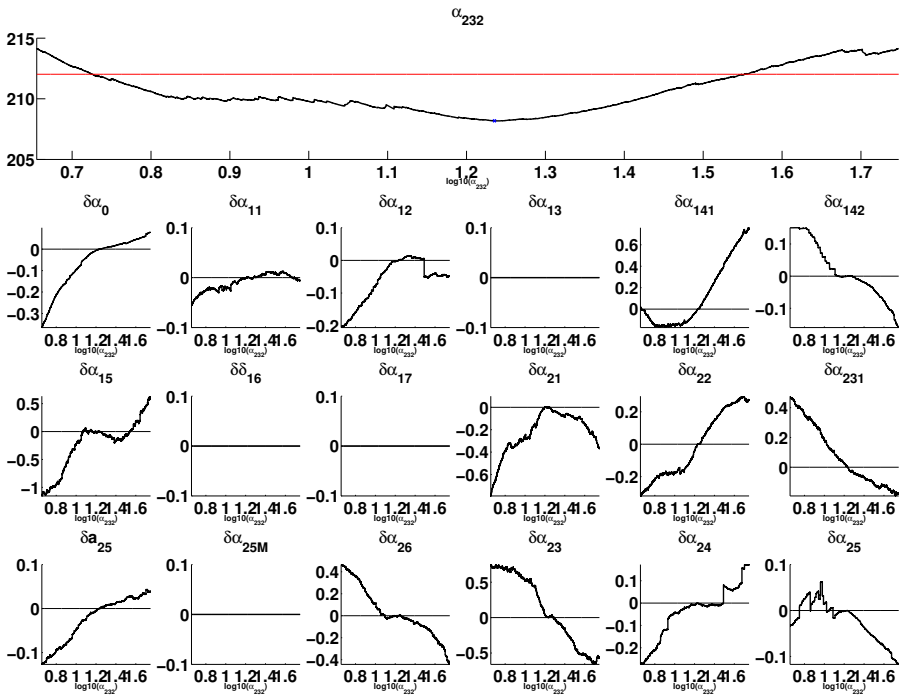

Supplementary Figure 14: Profile likelihood of model A2 for the specified kinetic parameter (upper panel, black line) and its dependencies on the remaining kinetic parameters in terms of relative change of each kinetic parameter in logspace (vertical axes of the small 3 x 6 subplots). The vertical axis in the upper panel indicates $\chi^2(\boldsymbol{\theta}_i)$, which is proportional to -2 times the profile likelihood value, whereas the horizontal axis represents the parameter value in logspace. The red line in the upper panel indicates the critical value for significance. The parameter value of the point estimate is indicated by a small blue cross in the upper panel.

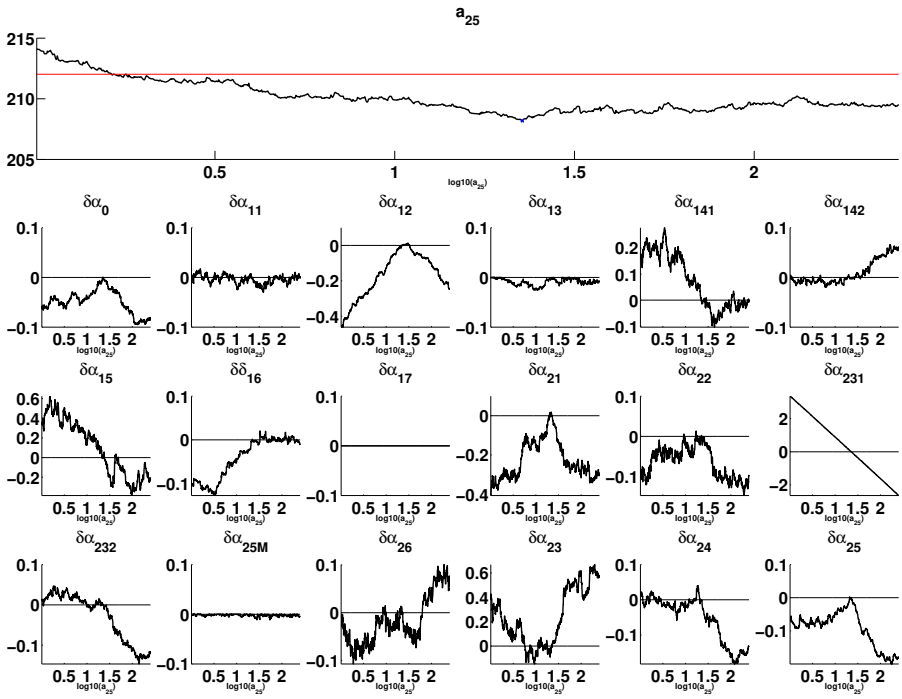

Supplementary Figure 15: Profile likelihood of model A2 for the specified kinetic parameter (upper panel, black line) and its dependencies on the remaining kinetic parameters in terms of relative change of each kinetic parameter in logspace (vertical axes of the small 3 x 6 subplots). The vertical axis in the upper panel indicates $\chi^2(\boldsymbol{\theta}_i)$, which is proportional to -2 times the profile likelihood value, whereas the horizontal axis represents the parameter value in logspace. The red line in the upper panel indicates the critical value for significance. The parameter value of the point estimate is indicated by a small blue cross in the upper panel.

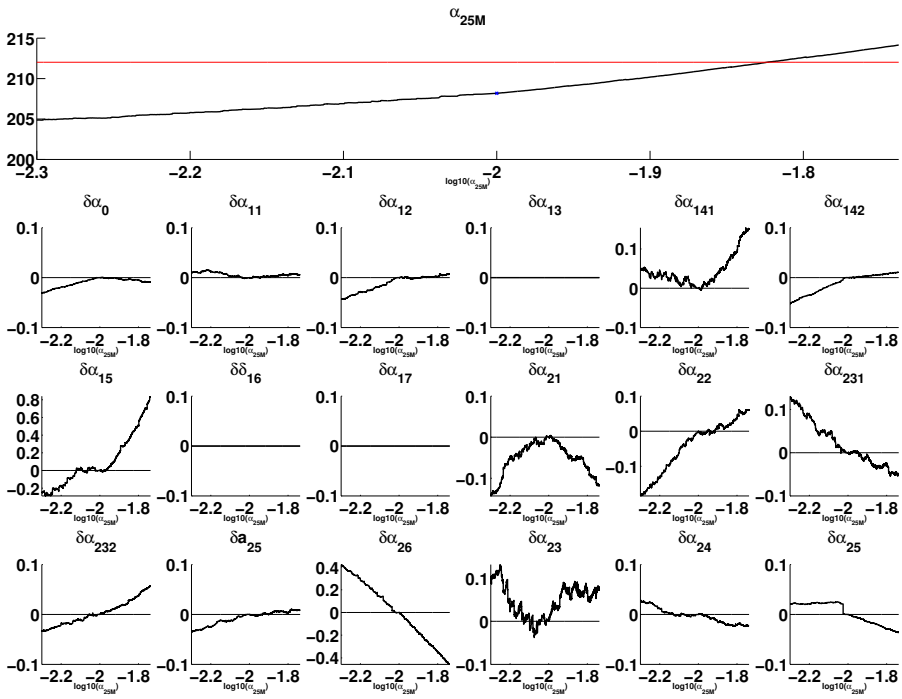

Supplementary Figure 16: Profile likelihood of model A2 for the specified kinetic parameter (upper panel, black line) and its dependencies on the remaining kinetic parameters in terms of relative change of each kinetic parameter in logspace (vertical axes of the small 3 x 6 subplots). The vertical axis in the upper panel indicates $\chi^2(\boldsymbol{\theta}_i)$, which is proportional to -2 times the profile likelihood value, whereas the horizontal axis represents the parameter value in logspace. The red line in the upper panel indicates the critical value for significance. The parameter value of the point estimate is indicated by a small blue cross in the upper panel.

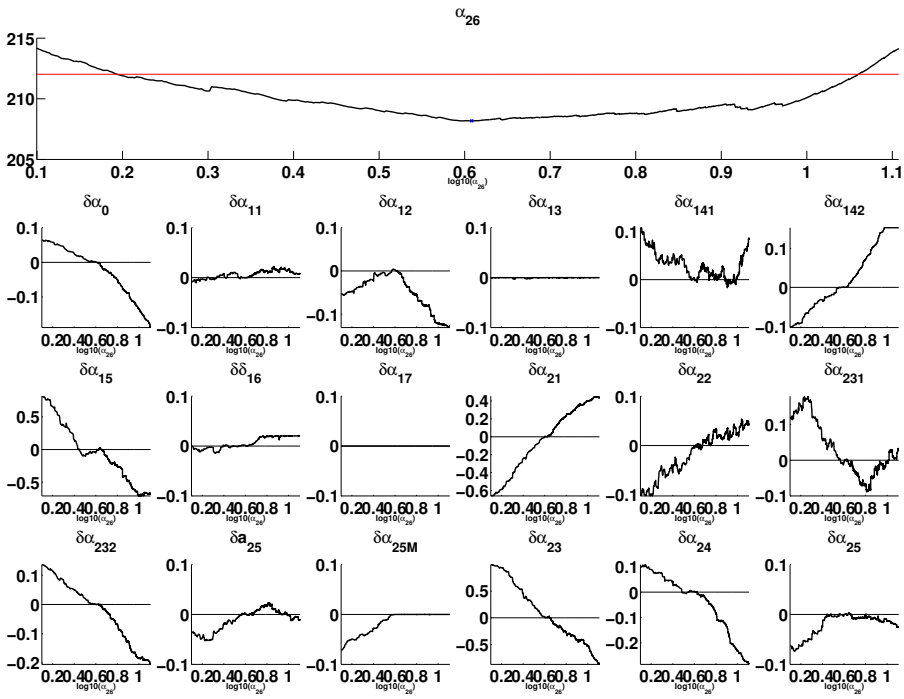

Supplementary Figure 17: Profile likelihood of model A2 for the specified kinetic parameter (upper panel, black line) and its dependencies on the remaining kinetic parameters in terms of relative change of each kinetic parameter in logspace (vertical axes of the small 3 x 6 subplots). The vertical axis in the upper panel indicates $\chi^2(\boldsymbol{\theta}_i)$, which is proportional to -2 times the profile likelihood value, whereas the horizontal axis represents the parameter value in logspace. The red line in the upper panel indicates the critical value for significance. The parameter value of the point estimate is indicated by a small blue cross in the upper panel.

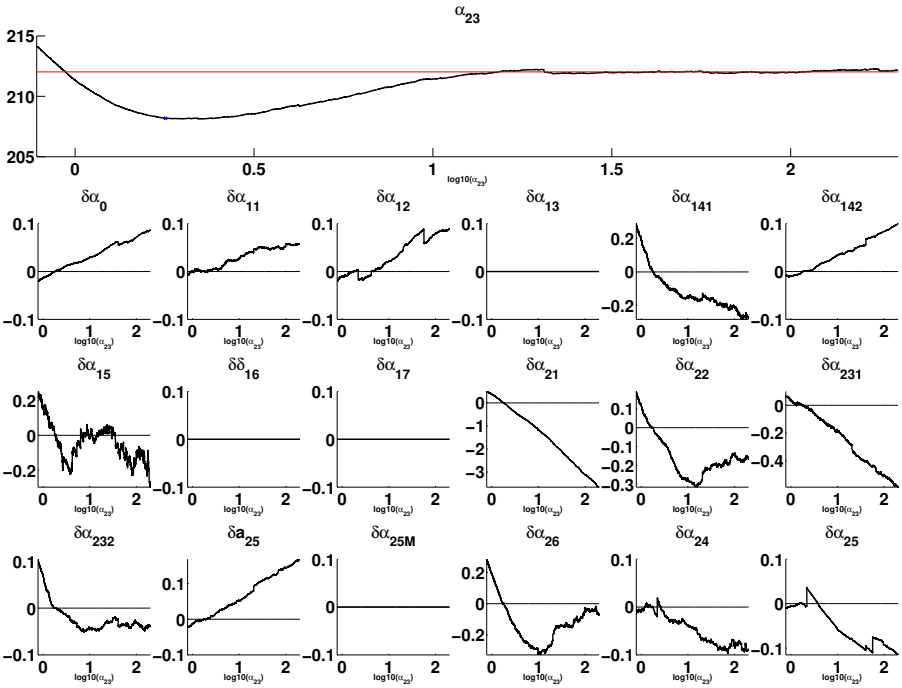

Supplementary Figure 18: Profile likelihood of model A2 for the specified kinetic parameter (upper panel, black line) and its dependencies on the remaining kinetic parameters in terms of relative change of each kinetic parameter in logspace (vertical axes of the small 3 x 6 subplots). The vertical axis in the upper panel indicates $\chi^2(\boldsymbol{\theta}_i)$, which is proportional to -2 times the profile likelihood value, whereas the horizontal axis represents the parameter value in logspace. The red line in the upper panel indicates the critical value for significance. The parameter value of the point estimate is indicated by a small blue cross in the upper panel.

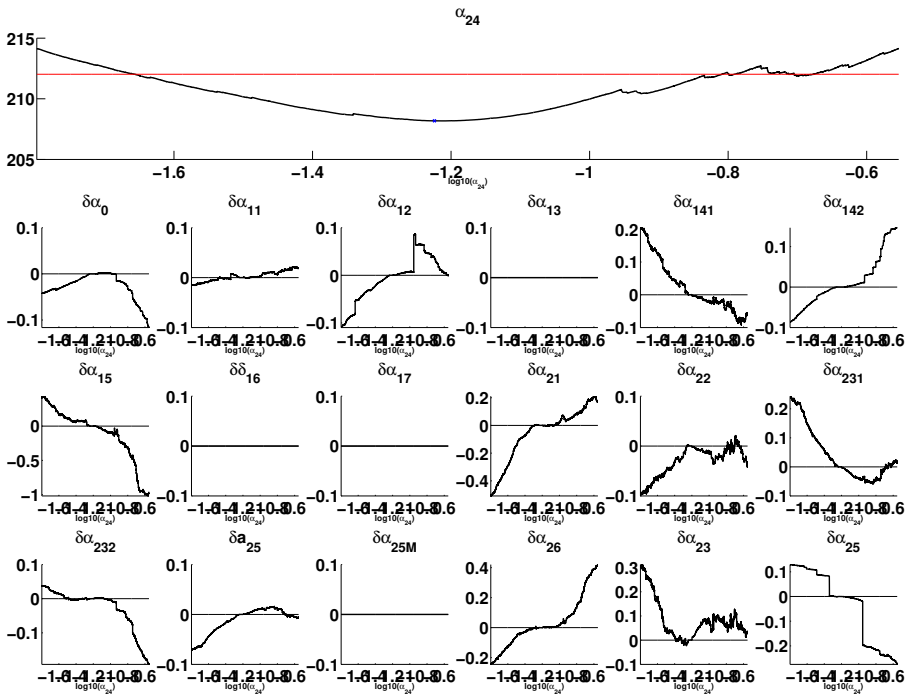

Supplementary Figure 19: Profile likelihood of model A2 for the specified kinetic parameter (upper panel, black line) and its dependencies on the remaining kinetic parameters in terms of relative change of each kinetic parameter in logspace (vertical axes of the small 3 x 6 subplots). The vertical axis in the upper panel indicates $\chi^2(\boldsymbol{\theta}_i)$, which is proportional to -2 times the profile likelihood value, whereas the horizontal axis represents the parameter value in logspace. The red line in the upper panel indicates the critical value for significance. The parameter value of the point estimate is indicated by a small blue cross in the upper panel.

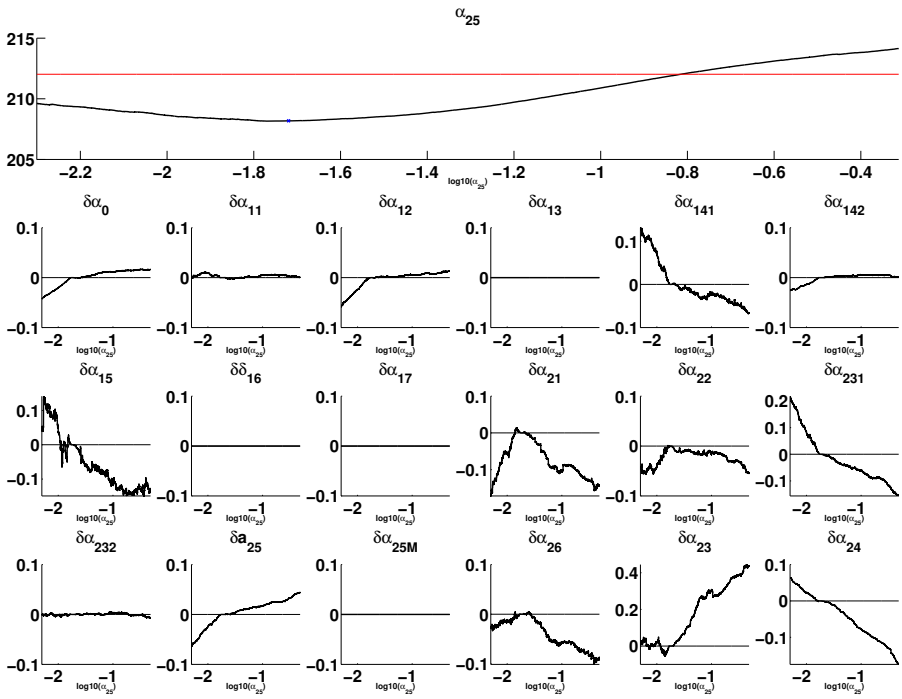

Supplementary Figure 20: Profile likelihood of model A2 for the specified kinetic parameter (upper panel, black line) and its dependencies on the remaining kinetic parameters in terms of relative change of each kinetic parameter in logspace (vertical axes of the small 3 x 6 subplots). The vertical axis in the upper panel indicates $\chi^2(\boldsymbol{\theta}_i)$, which is proportional to -2 times the profile likelihood value, whereas the horizontal axis represents the parameter value in logspace. The red line in the upper panel indicates the critical value for significance. The parameter value of the point estimate is indicated by a small blue cross in the upper panel.

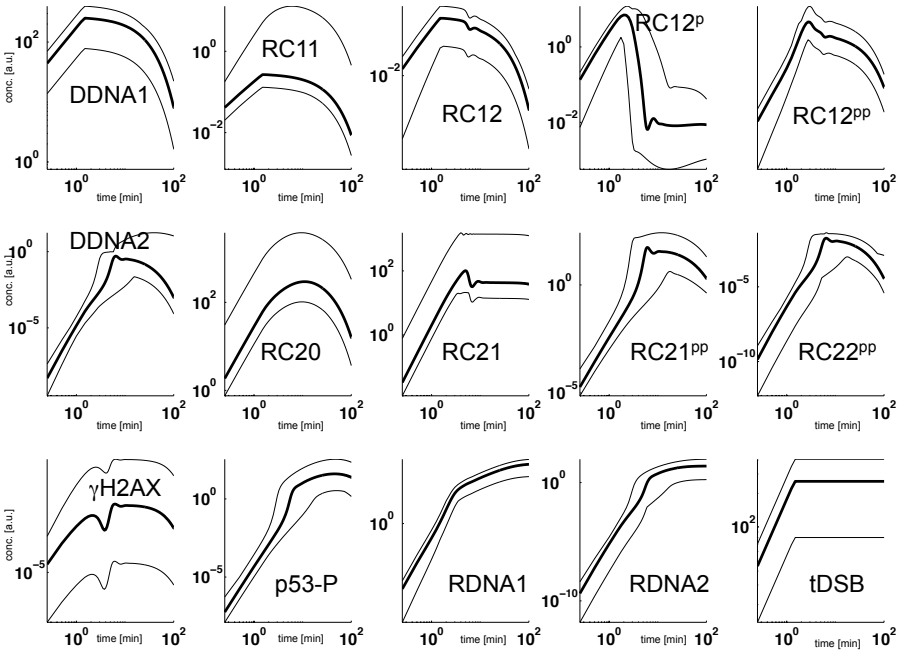

Supplementary Figure 21: Model states for a 5 Gy pulse and confidence bands (thin black lines) derived from the profile likelihood. For illustration purpose axes are on log-scale. The time window is from 0 to 100 minutes.

3 Generated Data Sets

Initial Data Set The initial data set represents time course data of γH2AX for 0.5, 1, 2, 5 and 40 Gy at a dose rate of 3.332 Gy/min including repetitions.

Supplementary Table 2: Part of the initial, processed data set including repetitions for γH2AX in arbitrary units at 0.5 Gy.

time [min]	replicate 1	replicate 2	replicate 3	mean	variance
0	0	0	0	0	0
30.0000	0.3392	0.5438	0.3223	0.4018	0.0152
90.0000	0.1149	0.4700	0.0561	0.2137	0.0502
180.0000	-0.0254	0.2590	-0.0634	0.0568	0.0310
300.0000	-0.0546	0.3194	-0.1082	0.0522	0.0543
720.0000	-0.3309	0.3717	-0.0962	-0.0185	0.1280

Supplementary Table 3: Part of the initial, processed data set including repetitions for γH2AX in arbitrary units at 1 Gy.

time [min]	replicate 1	replicate 2	replicate 3	mean	variance
0	0	0	0	0	0
30.0000	0.3416	0.1623	0.5049	0.3362	0.0294
90.0000	0.0844	-0.1095	0.0161	-0.0030	0.0097
180.0000	0.0231	-0.2766	-0.0151	-0.0895	0.0266
300.0000	0.1444	-0.3489	0.1186	-0.0286	0.0771
720.0000	0.1014	-0.8443	-0.2728	-0.3386	0.2268

Data Set for Optimal Design $\mathbf{D}_{\mathbf{I}}^{\star}$ The data set represents time course data of γH2AX for the optimized double pulse of 1 Gy at time $t = 0$ min and 20 Gy at time $t = 360$ min, both at a dose rates of 3.332 Gy/min including repetitions.

Supplementary Table 4: Part of the initial, processed data set including repetitions for γH2AX in arbitrary units at 2 Gy.

time [min]	rep. 1	rep. 2	rep. 3	rep. 4	rep. 5	mean	variance
0	0	0	0	0	0	0	0
30.0000	0.5681	0.9821	0.6178	0.3252	0.3657	0.5718	0.0684
90.0000	0.2436	0.6653	0.2415	0.0667	0.0634	0.2561	0.0602
180.0000	-0.0406	0.3705	0.0789	-0.0966	0.0236	0.0671	0.0331
300.0000	-0.0654	0.3057	0.1438	-0.2495	-0.2712	-0.0273	0.0626
720.0000	0.1207	0.4834	0.3147	-0.2747	-0.2334	0.0821	0.1109

Supplementary Table 5: Part of the initial, processed data set including repetitions for γH2AX in arbitrary units at 5 Gy.

time [min]	rep. 1	rep. 2	rep. 3	rep. 4	mean	variance
0	0	0	0	0	0	0
30.0000	0.3191	0.4677	0.2570	0.8668	0.4776	0.0751
90.0000	0.1627	0.0688	0.0179	0.4109	0.1651	0.0305
180.0000	-0.1855	-0.1512	-0.2190	0.3148	-0.0602	0.0633
300.0000	-0.0500	0.0001	-0.1764	-0.0034	-0.0574	0.0068
720.0000	-0.0641	-0.0230	-0.1582	0.7630	0.1294	0.1816

Supplementary Table 6: Part of the initial, processed data set including repetitions for γH2AX in arbitrary units at 40 Gy.

time [min]	rep. 1	rep. 2	rep. 3	rep. 4	mean	variance
0	0	0	0	0	0	0
30.0000	1.6426	1.0232	0.6457	0.8407	1.0381	0.1862
90.0000	1.7743	0.8925	0.6072	0.6837	0.9894	0.2883
180.0000	1.3355	0.6076	0.6076	0.2323	0.6957	0.2132
300.0000	1.1927	0.3388	0.4196	0.0833	0.5086	0.2286
720.0000	0.7881	-0.0271	0.2081	-0.1396	0.2074	0.1709

Supplementary Table 7: Processed data set including repetitions for γH2AX in arbitrary units for the optimized design $\mathbf{D}_{\mathrm{I}}^{\star}$.

time [min]	replicate 1	replicate 2	replicate 3	mean	variance
0	0	0	0	0	0
15.0000	0.2722	0.3709	0.1474	0.2635	0.0125
35.0000	0.1215	0.3145	0.1057	0.1806	0.0135
60.0000	-0.0805	0.3183	0.1245	0.1208	0.0398
160.0000	-0.2712	0.2290	0.0214	-0.0069	0.0632
240.0000	-0.1223	0.2553	-0.0195	0.0378	0.0381
370.0000	0.8405	0.7530	0.6690	0.7542	0.0074
420.0000	0.8336	0.6858	0.5358	0.6851	0.0222
450.0000	0.4571	0.6582	0.4958	0.5370	0.0114

Data Set p53-P from titration experiments P53-P data obtained for a double pulse of 1 Gy at time $t = 0$ min and 20 Gy at time $t = 360$ min.

Supplementary Table 8: Part of the initial, processed data set without repetitions for p53-P in arbitrary units for a double pulse of 1Gy and 20 Gy at time $t = 360$ min and application of 1μM Ku55933.

time [min]	rep. 1
0	0
35.0000	0.0253
370.0000	0.7520

Supplementary Table 9: Part of the initial, processed data set without repetitions for p53-P in arbitrary units for a double pulse of 1Gy and 20 Gy at time $t = 360$ min and application of 1μM Nu7441.

time [min]	rep. 1
0	0
35.0000	0.9234
370.0000	1.2692

Data Set for Optimal Design $\mathbf{D}^{\star}_{\mathbf{II}}$ The data set represents time course data of γH2AX for the optimized double pulse of 1 Gy at time $t = 0$ min and 20 Gy at time $t = 360$ min, both at a dose rates of 3.332 Gy/min and additional of (i) Nu7441 or Ku55933 or (ii) Nu7441 and Ku55933, including repetitions.

Supplementary Table 10: Part of processed data set including repetitions for γH2AX in arbitrary units for the optimized design $\mathbf{D}^{\star}_{\mathrm{II}}$ and application of 1μM Ku55933.

time [min]	replicate 1	replicate 2	mean	variance
0	0	0	0	0
15.0000	0.3000	0.2700	0.2850	0.0004
35.0000	0.0100	0.3300	0.1700	0.0512
60.0000	-0.0800	0.3300	0.1250	0.0841
160.0000	-0.1000	0.2300	0.0650	0.0545
240.0000	-0.2800	0.3900	0.0550	0.2245
370.0000	0.8900	0.9500	0.9200	0.0018
420.0000	0.8400	0.7700	0.8050	0.0024
450.0000	0.5300	0.5200	0.5250	0.0001

Supplementary Table 11: Part of processed data set including repetitions for γH2AX in arbitrary units for the optimized design $\mathbf{D}^{\star}_{\mathrm{II}}$ and application of 1μM Nu7441.

time [min]	rep. 1	rep. 2	rep. 3	rep. 4	mean	variance
0	0	0	0	0	0	0
15.0000	0.3700	0.1900	0.4500	0.2100	0.3050	0.0158
35.0000	0.6800	0.3400	0.2500	0.2300	0.3750	0.0436
60.0000	0.5800	-0.4200	0.2500	0.0500	0.1150	0.1750
160.0000	0.4100	-0.6800	-0.0100	-0.1600	-0.1100	0.2026
240.0000	0.4400	0.3400	0.2100	-0.0700	0.2300	0.0489
370.0000	1.5200	1.2300	1.3900	0.7700	1.2275	0.1071
420.0000	1.4100	1.1300	1.6300	0.6100	1.1950	0.1940
450.0000	0.9800	0.7800	1.3000	0.4800	0.8850	0.1188

Supplementary Table 12: Part of processed data set including repetitions for γH2AX in arbitrary units for the optimized design $\mathbf{D}^{\star}_{\mathrm{II}}$ and application of 1μM of Nu7441 and Ku55933.

time [min]	rep. 1	rep. 2	rep. 3	rep. 4	mean	variance
0	0	0	0	0	0	0
15.0000	0.1119	0.0506	0.2943	0.4913	0.2370	0.0394
35.0000	0.2939	0.1965	0.0905	0.6053	0.2966	0.0493
60.0000	0.0471	0.1236	0.0536	0.4099	0.1586	0.0293
160.0000	0.1789	0.1765	0.0223	0.2594	0.1593	0.0098
240.0000	-0.1896	0.1048	-0.0220	0.2791	0.0431	0.0393
370.0000	0.3661	0.7154	0.4716	0.8790	0.6080	0.0540
420.0000	0.1236	0.6413	0.4935	0.6847	0.4858	0.0650
450.0000	0.0028	0.4965	0.4070	0.5080	0.3536	0.0567

References

Julie Bachmann, Andreas Raue, Marcel Schilling, Martin Boehm, Clemens Kreutz, Martin Bhm, Daniel Kaschek, Hauke Busch, Norbert Gretz, Wolf Lehmann, Jens Timmer, and Ursula Klingmueller. Division of labor by dual feedback regulators controls jak2/stat5 signaling over broad ligand range. *Molecular Systems Biology*, 7:516, 2011. ISSN 1744-4292.

I. Brandsma and D. C. Gent. Pathway choice in dna double strand break repair: observations of a balancing act. *Genome Integr*, 3(1):9, 2012.

C. E. Canman, D. S. Lim, K. A. Cimprich, Y. Taya, K. Tamai, K. Sakaguchi, E. Appella, M. B. Kastan, and J. D. Siliciano. Activation of the atm kinase by ionizing radiation and phosphorylation of p53. *Science*, 281(5383):1677–9, 1998.

Doug W. Chan, Benjamin Ping-Chi Chen, Sheela Prithivirajsingh, Akihiro Kurimasa, Michael D. Story, Jun Qin, and David J. Chen. Autophosphorylation of the dna-dependent protein kinase catalytic subunit is required for rejoining of dna double-strand breaks. *Genes Development*, 16(18):2333–2338, 2002.

Benjamin P. C. Chen, Naoya Uematsu, Junya Kobayashi, Yaniv Lerenthal, Andrea Krempler, Hirohiko Yajima, Markus Lbrich, Yosef Shiloh, and David J. Chen. Ataxia telangiectasia mutated (atm) is essential for dna-pkcs phosphorylations at the thr-2609 cluster upon dna double strand break. *Journal of Biological Chemistry*, 282(9): 6582–6587, 2007.

F. A. Cucinotta, J. M. Pluth, J. A. Anderson, J. V. Harper, and P. O'Neill. Biochemical kinetics model of dsb repair and induction of gamma-h2ax foci by non-homologous end joining. *Radiat. Res.*, 169(2):214–22, 2008.

Xiaoping Cui, Yaping Yu, Shikha Gupta, Young-Moon Cho, Susan P. Lees-Miller, and Katheryn Meek. Autophosphorylation of dna-dependent protein kinase regulates dna end processing and may also alter double-strand break repair pathway choice. *Molecular and Cellular Biology*, 25(24):10842–10852, 2005.

David O. Ferguson, JoAnn M. Sekiguchi, Sandy Chang, Karen M. Frank, Yijie Gao, Ronald A. DePinho, and Frederick W. Alt. The nonhomologous end-joining pathway of dna repair is required for genomic stability and the suppression of translocations. *Proceedings of the National Academy of Sciences*, 97(12):6630–6633, 2000.

Ryan N. Gutenkunst, Joshua J. Waterfall, Fergal P. Casey, Kevin S. Brown, Christopher R. Myers, and James P. Sethna. Universally sloppy parameter sensitivities in systems biology models. *PLoS Comput Biol*, 3(10):e189, 2007.

Alan C. Hindmarsh, Peter N. Brown, Keith E. Grant, Steven L. Lee, Radu Serban, Dan E. Shumaker, and Carol S. Woodward. SUNDIALS: Suite of nonlinear and differential/algebraic equation solvers. *ACM Trans. Math. Softw.*, 31(3):363–396, September 2005. ISSN 0098-3500. doi: 10.1145/1089014.1089020.

G. S. Jimenez, F. Bryntesson, M. I. Torres-Arzayus, A. Priestley, M. Beeche, S. Saito, K. Sakaguchi, E. Appella, P. A. Jeggo, G. E. Taccioli, G. M. Wahl, and M. Hubank. Dna-dependent protein kinase is not required for the p53-dependent response to dna damage. *Nature*, 400(6739):81–3, 1999.

Sabrina Koecher, Thorsten Rieckmann, Gabor Rohaly, Wael Y. Mansour, Ekkehard Dikomey, Irena Dornreiter, and Jochen Dahm-Daphi. Radiation-induced double-strand breaks require atm but not artemis for homologous recombination during s-phase. *Nucleic Acids Research*, 2012.

C. Kreutz, M. M. Bartolome Rodriguez, T. Maiwald, M. Seidl, H. E. Blum, L. Mohr, and J. Timmer. An error model for protein quantification. *Bioinformatics*, 23(20): 2747–2753, 2007.

S. P. Lees-Miller, K. Sakaguchi, S. J. Ullrich, E. Appella, and C. W. Anderson. Human dna-activated protein kinase phosphorylates serines 15 and 37 in the amino-terminal transactivation domain of human p53. *Molecular and Cellular Biology*, 12(11):5041–9, 1992.

Eckhard Limpert, Werner A. Stahel, and Markus Abbt. Log-normal distributions across the sciences: Keys and clues. *BioScience*, 51(5):341–352, 2001.

Marta Martin, Anna Genesca, Laura Latre, Isabel Jaco, Guillermo E. Taccioli, Josep Egozcue, Maria A. Blasco, George Iliakis, and Laura Tusell. Postreplicative joining of dna double-strand breaks causes genomic instability in dna-pkcsdeficient mouse embryonic fibroblasts. *Cancer Research*, 65(22):10223–10232, 2005.

Ciaran Morrison, Eiichiro Sonoda, Noriaki Takao, Akira Shinohara, Ken-ichi Yamamoto, and Shunichi Takeda. The controlling role of atm in homologous recombinational repair of dna damage. *EMBO Journal*, 19(3):463–471, 2000.

Kazunari Mouri, Jose C. Nacher, and Tatsuya Akutsu. A mathematical model for the detection mechanism of dna double-strand breaks depending on autophosphorylation of atm. *PLoS ONE*, 4(4):e5131–, 2009.

Jessica A. Neal and Katheryn Meek. Choosing the right path: Does dna-pk help make the decision? *Mutation Research/Fundamental and Molecular Mechanisms of Mutagenesis*, 711(12):73–86, 2011.

A Raue, C Kreutz, T Maiwald, J Bachmann, M Schilling, U Klingmueller, and J Timmer. Structural and practical identifiability analysis of partially observed dynamical models by exploiting the profile likelihood. *Bioinformatics*, 25(15):1923–9, 2009. ISSN 1367-4803.

Caroline A. Schneider, Wayne S. Rasband, and Kevin W. Eliceiri. Nih image to imagej: 25 years of image analysis. *Nat Meth*, 9(7):671–675, 2012.

Sheau-Yann Shieh, Masako Ikeda, Yoichi Taya, and Carol Prives. Dna damage-induced phosphorylation of p53 alleviates inhibition by mdm2. *Cell*, 91(3):325–334, 1997.

Meena Shrivastav, Cheryl A. Miller, Leyma P. De Haro, Stephen T. Durant, Benjamin P. C. Chen, David J. Chen, and Jac A. Nickoloff. Dna-pkcs and atm co-regulate dna double-strand break repair. *DNA Repair*, 8(8):920–929, 2009.